Technical Report

Title: *Analyses of DGR-1, DGR-2, DGR-3 and DGR-4 Borehole Images for Stress Characterization*

Document ID: TR-08-35

Authors: Benoît Valley & Sean Maloney, MIRARCO Mining Innovation

Revision: 1

Date: January 28, 2010

INTERA

Intera Engineering DGR Site Characterization Document	
Title:	Analyses of DGR-1, DGR-2, DGR-3 and DGR-4 Borehole Images for Stress Characterization
Document ID:	TR-08-35
Revision Number:	1 Date: January 28, 2010
Authors:	Benoît Valley & Sean Maloney, MIRARCO Mining Innovation
Technical Review:	Michael Melaney, Kenneth Raven, Dougal McCreath (Laurentian University); Tom Lam (NWMO)
QA Review:	John Avis
Approved by:	Kenneth Raven

Document Revision History		
Revision	Effective Date	Description of Changes
0	October 21, 2009	Initial Release
1	January 28, 2010	Updated Figure 2 for revised lithological logs (TR-08-12), revised presentation of Figure 16 to rose diagrams. Minor editorial text revisions in Sections 1.1, 2.3.1, 3.2, 3.3.2 and 6. Revisions to captions for Figures 15 and 16.

TABLE OF CONTENTS

LIST OF TABLES

LIST OF APPENDICES

1   Introduction

1.1   Objective

The Bruce site is located in the Municipality of Kincardine, Ontario. Boreholes DGR-1, DGR-2, DGR-3 and DGR-4 were drilled as part of the Geoscientific Site Characterization Plan (GSCP, Intera Engineering Ltd., 2006), a step-wise four year program consisting of several phases, being conducted at the Bruce site. The purpose of the GSCP is to assess the suitability of the Bruce site to construct a Deep Geologic Repository (DGR), a long-term management facility for low and intermediate level nuclear waste only. The DGR would be constructed at a depth of about 680 m in low permeability limestone.

During the GSCP for the DGR, knowledge of regional stress magnitudes and directions is needed for numerical modeling of the excavation response to applied mechanical loads and long term evaluation. Where little data concerning the in-situ stress state at depth exists, such as in the sedimentary rocks of the Paleozoic era at the Bruce site, indirect means of inferring or constraining stress orientation and magnitude must be adopted for preliminary studies. One such means involves observing the physical response of deep boreholes.

The purpose of this study is to review the data available from boreholes DGR-1, DGR-2, DGR-3 and DGR-4 at the Bruce site with the objective of constraining the possible range of the in-situ stress state at the level of the DGR. The work described in this Technical Report complements and enhances previous work done on boreholes DGR1 and DGR-2 (Intera Engineering Ltd., 2009a). All figures for this report are provided in Appendix A.

1.2   Approach

Two features, occasionally observed in boreholes, can be used to ascertain the orientation of the principal stresses and constrain their magnitudes (Figure 1): breakouts (Bell and Gough, 1979) and drilling induced fractures (Brudy and Zoback, 1999). Breakouts typically manifest as pairs of diametrically-opposite spall zones that extend along the borehole axis (Figure 1b). They occur when the local value of tangential compressive stress at the borehole wall exceeds the rock strength. In the simple case of a vertical borehole penetrating a rock mass in which one principal stress is vertical, breakouts, if they occur, indicate the orientation of the minimum horizontal stress

Drilling induced tension fractures (DITFs) form where the net tangential stress distribution around the hole is sufficiently tensile at some point to produce failure (Figure 1c). The net tangential stress is the sum of a tensile cooling component, which is axially-symmetric, and the natural wellbore stress concentration arising from the 'far-field' stresses, which are not necessarily axially-symmetric and may be everywhere compressive. In the case of a vertical borehole penetrating a medium in which one principal stress is also vertical, the least compressive value of the circumferential stress variation about the borehole due to the far field stresses occurs in the direction of the maximum horizontal stress. Thus, it is in this direction that the greatest tension develops and a pair of diametrically-opposite DITFs forms. If the borehole axis is aligned with a principal stress, they will tend to be axial. We denote these as A-DITFs. However, in the case where the borehole axis is not aligned with a principal axis, the criterion for tensile failure might still be met but then DITFs will tend to form as a stack of en-echelon, induced fractures. We denote these as E-DITFs. The relationship between the induced fracture geometry and the in-situ stress orientations and magnitudes in this case is not as simple as in the aligned case.

In a first stage, the borehole image is investigated to identify the presence of breakouts or DITFs. This is done firstly by visual inspection of the images, but also by automatic borehole ellipticity detection. In a second phase, the presence or the absence of wellbore failure is used to put constraints on stress magnitudes. In order to constrain stresses, an estimation of the strength of the materials is needed. Lab testing of core samples allows

INTERA

us to estimate this strength. However, it is worthy to note a change in the approach of dealing with these strength estimates compared to the previous work completed (Intera Engineering Ltd., 2009a). Previously, we dealt with strength in a deterministic manner. In the present work, we used a probabilistic approach to better account for the variability of the strength distributions.

2   Analysis of Borehole DGR-1, DGR-2, DGR-3 and DGR-4 Images

2.1   Borehole Description

Boreholes DGR-1, DGR-2, DGR-3 and DGR-4 were drilled to approximate depths of 462, 862, 869 and 857 mBGS, respectively, mostly through a sedimentary series of Ordovician to Devonian rocks (see Table 1 and Figure 2). Wellhead coordinates are given in Table 1. DGR-1 and DGR-2 are collared from almost the same location. DGR-3 is located about 1.1 km west of DGR-1 and DGR-2; DGR-4 is collared 1.2 km northwest of DGR-1 and DGR-2. Every borehole has a multi-section layout with telescoping holes and casing sizes. Details of the borehole layout are given in Table 1and schematically in Figure 2. The boreholes are sub-vertical, never exceeding a tilt of 1.5°, 1°, 4.5° or 4°, for DGR-1, DGR-2, DGR-3 or DGR-4, respectively. Formations and lithologies are also displayed in Figure 2. Correlation of formations and lithologies between boreholes shows a depth mismatch due to the various collar heights, to their location relative to the southwest dipping sedimentary stack and to minor thickness variations in the stratigraphic series. However, the mismatch rarely exceeds about 20 m. In the context of the present study and for the sake of simplicity, it was deemed acceptable to display and match the data from all boreholes according to their own depth scale. However, special care is taken when averaging rock properties of overlapping sections in order to avoid the mixing of different rock types.

Table 1   Borehole Technical Details, Wellhead Coordinates and Total Depths

Casing String/Borehole	Bottom Depth	Borehole Diameter		Casing Size	
	(mBGS)	(inch)	(mm)	(inch)	(mm)
DGR-1 N 4907753.243 E 454239.777 185.7 mASL					
surface casing	23.3	17 1/2	445	13 3/8	340
intermediate casing # 1	182.3	12 1/2	318	9 5/8	245
main borehole	462.9	6 1/4	159	open hole	
DGR-2 N 4907720.300 E 454208.921 185.8 mASL					
surface casing	23.4	24	610	20	508
intermediate casing # 1	189.2	17 1/2	445	13 3/8	340
intermediate casing # 2	450.7	12 1/2	318	9 5/8	245
main borehole	862.3	6 1/4	159	open hole	
DGR-3 N 4907739.8 E 453080.5 187.4 mASL					
surface casing	8.9	15	381	12 3/4	324
intermediate casing # 1	30.2	11 5/8	295	9 5/8	245
intermediate casing # 2	208.5	8 3/4	222	7	178
main borehole	869.2	5 5/8	143	open hole	
DGR-4 N 4908743.9 E 453378.3 181.6 mASL					
surface casing	8.6	15	381	12 3/4	324
intermediate casing # 1	30.2	11 5/8	295	9 5/8	245
intermediate casing # 2	188.7	8 3/4	222	7	178
main borehole	857.0	5 5/8	143	open hole	

INTERA

The lithologies consist exclusively of sedimentary rocks, mostly carbonates and shales. Below the surficial deposits, the upper section of the borehole down to about 190 mBGS is mostly within dolostones or cherty dolostones. From 190 to 370 mBGS (Salina Formation), a shale component, sometimes dominant, is present. It is accompanied with some brecciaed layers, as well as some anhydritic layers. Below the Salina Formation, down to 410 mBGS (Fossil Hill Formation), dolostone or dolomitic limestone are the dominant lithologies. From 410 to 660 mBGS, the prominent rock types are shales with some limestone/shale interbedding. Below 660 mBGS, the dominant rock type is limestone with varying clay content (marls), with a general trend of less clay content going downwards.

2.2 Data Description

2.2.1 Acoustic Borehole Images

The primary sources of information for the present study are borehole wall images acquired with an acoustic televiewer. These images allow for the assessment of borehole wall failure. All the images are presented in Figure 3. All four holes have been extensively logged with various geophysical tools, including the acoustic televiewer. Acoustic borehole wall images were acquired with an ABI40 probe from ALT for the depths 180.5 to 462.5 mBGS in DGR-1, 450.3 to 836.9 mBGS in DGR-2, 206.4 to 849.0 mBGS in DGR-3 and 186.2 to 838.8 mBGS in DGR-4. The axial sampling along each borehole was about 3 mm and the azimuthal sampling was 2.5° (144 measurements for each revolution). In DGR-3, the images were acquired in two logs overlapping at 319 mBGS. The transit times were converted to borehole radius assuming a borehole fluid velocity of 1680 m/s for DGR-1 and DGR-2 (probe parameters are 20 mm for tool radius and 75μs two-way travel time in the probe). The fluid velocity was derived by back analyzing the average acoustic caliper log provided by Intera Engineering Ltd. As will be shown later, this velocity seems to be appropriate for DGR-1, but is possibly too high for DGR-2. For DGR-3, the fluid velocity was estimated to be 1623 m/s for the upper section and 1792 m/s for the lower section. A fluid velocity of 1975 m/s was used for analysis of the DGR-4 image.

For this reason, the caliper computation is not precise and is anyway influenced by the variation in fluid characteristics along the hole which were high for DGR-3 and DGR-4. These uncertainties have no impact on our analysis, because we are interested only in the relative shape of the borehole section, not the absolute size. No centralization was applied to the images because the centralization algorithm provided in the image processing software, WellCAD, is not shape preserving which could induce bias in the borehole section shape analysis performed here.

2.2.2 Rock Properties Data

Rock testing data used in this study are Unconfined Compressive Strength (UCS), Young's modulus and density summarized from the reports: TR-07-03 (Intera Engineering Ltd., 2009b), TR-08-11 (Intera Engineering Ltd., 2009c, and TR-08-24 (Intera Engineering Ltd., 2009d). In-situ density logs acquired in all three boreholes are also included.

2.3 Wellbore Wall Failure Inspection

2.3.1 Drilling Induced Tension Fractures

Drilling induced tension fractures can include axial fractures generated parallel to the borehole axis or stacks of en-echelon fractures occurring at an angle to the borehole axis. These two types of drilling induced fractures are reflective of different principal stress conditions (Brudy and Zoback, 1999). They are sometimes difficult to distinguish from natural fractures (existing before drilling). Axial drilling induced tension fractures can be confused with sub-vertical natural fractures intercepting the borehole at a low angle. En-echelon drilling induced tension fractures can be misinterpreted when a series of steep, parallel, natural fractures are present.

In borehole DGR-1, borehole parallel features were encountered at two depths. These two examples are presented in Figures 4a and 4b. In the first case, comparison with core photos clearly showed the presence of pre-existing sub-vertical veins and so the occurrence of DITFs was discarded. In the second case, a sub-vertical fracture was also seen in the cores, though not as readily apparent. Another example of a drilling induced tension fracture like feature was also found in DGR-4 (Figure 4c), but here also, examination of the core photo allows us to discard the occurrence of DITFs. Consequently, it was concluded that no evidence of drilling induced tensile failure was present in the acoustic televiewer log for any borehole.

2.3.2 Breakouts

Breakouts form pairs of spall zones resulting in an elongated borehole section. Breakouts may be confused with other borehole enlargements that are not induced by stress-driven failure of the borehole wall. These include borehole mechanical wearing induced by friction with the drill string and local failure controlled by the natural fracture geometry (example from DGR-2 in Figure 4d).

No breakouts were identified along boreholes DGR-1, DGR-2, DGR-3 and DGR-4. However, some zones with borehole enlargement are present as highlighted by the caliper logs acquired in each borehole (see Figure 5). This is the case for the Salina Formation above 300 mBGS, where the diametrical enlargement exceeds 2 cm. Some systematic enlargements (less than 1 cm) are also present for the depth range 660 to 780 mBGS (argillaceous limestone from the Cobourg, Sherman Fall and Kirkfield Formations). Such borehole enlargements are commonly called wash-outs and are mainly due to drilling-induced mechanical disturbance and erosion by the drilling fluid of weak and water sensitive lithologies. Stress concentration effects can also partially contribute to these borehole enlargements, but the characteristic features of stress-induced failure will be masked by the mechanical and hydraulic effects.

2.3.3 Borehole Ellipticity Analysis

The borehole shape was systematically analyzed in order to identify possible borehole elongations which were not captured during the visual inspection of the images. The general principle of this analysis is to fit ellipses on borehole sections derived from the acoustic travel time.

In detail, the analysis was performed every 5 cm axially, averaging radius information over a 10 cm window. Thus two successive analyses have a 5 cm overlap. The vertical sampling of borehole radius being 3 mm, each window contains 33 borehole sections. The advantage of averaging over a depth window is that it permits reduction of the noise (bad picks in the recordings of the rebounding acoustic waves resulting in an erroneous borehole radius). Radius measurements smaller than 65 mm for DGR-1 and DGR-2 and 45 mm for DGR-3 and DGR-4 were discarded and outliers were removed using an iterative implementation of the Grubbs' test (Grubbs, 1969) before averaging. The noise removal is an important stage of the analysis, because the best ellipse fitting process may be significantly perturbed by outliers. Best fit ellipses were obtained by a stable, direct, least square method (Halir and Flusser, 1998). The outputs of the analysis are the lengths of the ellipse's long and short axes as well as the orientation.

The results of this analysis are presented in Figure 6. The length difference between both ellipse axes is less than 0.5% for most of the borehole length, indicating that the borehole sections are fairly circular. There is one major exception to this around 260 mBGS, within the Salina Formation, where the length difference reaches 2.5% in DGR-1, 2% in DGR-3 and 4% in DGR-4 (observation in qualitative and quantitative agreement with caliper data of Figure 5). A less pronounced elongation is also systematic for all boreholes in the Ordovician limestones of the Cobourg, Sherman Fall and Kirkfield Formations located approximately from 660 to 760 m.

The orientations of the ellipses are also presented in Figure 6c, 6d and 6e. In DGR-1 and DGR-2, for most of the borehole length, the orientation is erratic, with an exception occurring in the depth range 660 to 760 mBGS,

where a systematic, SE oriented (138°), slight borehole elongation is noticed. This depth range corresponds to the limestones of the Ordovician Cobourg, Sherman Fall and Kirkfield Formations. In the Salina Formation, where the ratios between ellipse axes are higher, the orientation is not stable.

In borehole DGR-3 the ellipse orientation are more systematically organized and can be summarize in four depth sections:

1)   down to 380 mBGS: systematic ESE (109°) orientation. Note that the borehole azimuth has also a stable ESE orientation for this section.

2)   380 to 530 mBGS: systematic SE orientation (127°), not exactly aligned, but again fairly close to borehole azimuth.

3)   530 to 680 mBGS: erratic ellipse orientation

4)   680 to 780 mBGS: systematic SE orientation (141°). There is a large offset with respect to the borehole azimuth which is about ENE (65°) at this depth.

It is possible that the generally better organized ellipse orientation in DGR-3 compared to other boreholes is related to the fairly stable DGR-3 borehole trajectory.

In DGR-4, the behavior is very similar to that of DGR-1/DGR-2 with mostly erratic ellipse orientation except for the depth range 660 to 760 mBGS where a systematic SE (131°) is apparent.

One possible reason for the preferential elongation orientation in the Ordovician argillaceous limestones could be mechanical wearing of the borehole walls, if the borehole was sufficiently inclined and oriented in the same direction as the borehole elongation. However, comparison of the elongation (black curves in Figures 6c, 6d, and 6e) and the borehole trajectory (dashed curves) indicates that this is not the case. Thus, the possibility that the systematic SE borehole elongation in the Ordovician argillaceous limestones of the Cobourg, Sherman Fall and Kirkfield Formations is stress remains, however, the exact mechanism (purely elastic response, stress-induced creep, limited failure) cannot be defined.

3   Evaluation of Possible Stress States Compatible with Observations

3.1   Vertical Stress Magnitude

The presence of axial, drilling induced, tension fractures along vertical borehole sections would indicate that one principal stress is vertical. However, the presence of en-echelon drilling induced tension fractures would indicate that one principal stress deviates from vertical. In the case of DGR-1, DGR-2, DGR-3 and DGR-4, no drilling tensile fractures are present and a direct assessment of principal stress verticality is not possible. We have to accept the unconfirmed hypothesis that one principal stress is vertical. This hypothesis is generally acceptable when the area of concern is deep enough to be unaffected by topographical effects and outside the local perturbing effect of major faults.

Accepting that one principal stress is vertical, we can estimate its magnitude by integrating the rock density with depth. The density of 189 core samples has been measured for the depth ranging from 27.3 to 737.2 mBGS (see Figure 7a). Compensated density logs have been also acquired in each borehole and are displayed in Figure 7a. The density logs values are generally slightly higher than that measured on cores. In Figure 7b, a mean density with standard deviation is computed including both lab and in-situ measurements using a 20 m sliding window. When both lab and in-situ data are available within an averaging window, the same weight is given to both data types. Integration of compiled density data and linear best fit over the depth of interest lead to

the following relation for vertical stress magnitude:

$$S_v[MPa] = 26.3 * depth[km] \qquad\qquad (1)$$

At 700 mBGS depth, the uncertainty (±1std) is about 1 MPa.

3.2   Pore Pressure and Borehole Pressure

For the sake of simplicity, the pore pressure was considered to be hydrostatic with a water level at ground surface. More likely, the actual water level is slightly lower. If the water level was actually 10 mBGS, our profile would overestimate the actual pore pressure by only 0.1 MPa. The pore pressure is then given by the following relation:

$$P_p[MPa] = 9.81 * depth[km] \qquad\qquad (2)$$

Actual pore pressure measurements acquired between April and June 2008 in DGR-1 and DGR-2 suggest that the pore pressure profile is more complicated. Roughly, the pore pressure is less than hydrostatic between 480 and 760 mBGS and more than hydrostatic between 385 and 415 mBGS and below 760 mBGS. However the maximum difference to hydrostatic is only about 2 MPa. The induced uncertainty on the stress estimate, through the effective stress for compressive failure, will be of the same amount.

The borehole pressure is dictated by the density of the drilling fluid and its level within the borehole. Drilling fluid density records for DGR-3 and DGR-4 show that drilling fluid density varies from 1000 kg/m^3 to 1110 kg/m^3. The difference in pressure induced by these drilling fluids compared to fresh water is always less than 1 MPa. Excess borehole pressure will tend to stabilize the borehole walls and reduce or inhibit the formation of breakouts. It has also to be assumed that the borehole was not always filled with water. Particularly while tripping the drill string out of hole, it is expected that the drilling fluid level in the borehole drops and that pressure in the borehole is reduced. This situation will promote the formation of breakouts. Here again, the effect on stress magnitude estimate should be less than 1 MPa.

3.3   Horizontal Stress Magnitudes

Estimates of the horizontal stress magnitudes were derived from the analysis of the maximum stress conditions that could exist without causing failure of the borehole wall. Since the absence of failure depends on the rock strength, the rock strength is considered first.

3.3.1   Review of Strength Data

Ultimate strength data obtained from uniaxial compressive tests available at the time of preparation of this Technical Report are presented in Figure 8a. Strength varies considerably over the borehole depth, particularly when changing rock type. A strength profile was derived by averaging strength using a 30 m moving window. Mean and standard deviation are computed for each window; the latter is discarded if based on less than 5 data points. Where no data are available, a piecewise cubic Hermite interpolation is used. The so-compiled strength profile with standard deviation is presented in Figure 8b.

The same processing logic was applied to the stiffness (Young's modulus) data and the results are presented in Figure 9. Strength and stiffness variations are clearly correlated. Such a correlation was used by Deere (1968) to propose a rock classification scheme. The data are in agreement with Deere's classification with medium to high strength for limestone/dolostone, and very low to medium strength for shales (see Figure 10).

A serious flaw in the proposed strength profile is the assumption that strength is normally distributed and the subsequent way that standard deviation is interpolated where there is insufficient data. For low strength rocks, this results in negative strength for the lower tail of the distribution which is not realistic (e.g. around 260 mBGS). Moreover, because we are assessing the absence of failure, the strength at the lower end of the distribution is critical. For low strength rocks, using normally distributed strengths, borehole failure, even with zero stresses at the borehole wall, would be predicted. In order to avoid this problem different approaches are possible:

- Keeping a normal distribution for rock strength but limiting the standard deviation to 25% of the mean strength where mean strength is very low and where insufficient data are available to properly constrain the strength variability

- Using an alternate distribution type; for example log-normal or beta distribution

These various approaches have been compared and in the present case lead to similar results in terms of constraints on stresses. In the following, the approach using a log-normal distribution for strength will be used to assess borehole failure. The log-normal parameters are derived in the same way as for Figure 8. Generally, the downside to this approach is that the log-normal assumption will tend to over-estimate strength on the high end of the distribution. However, this is not critical at all for our case as we are considering only the absence of failure (the lower end of the distribution).

3.3.2 Evaluation of Horizontal Stress Magnitudes

Generally, the stress in the crust is limited by the shear strength of critically oriented faults. A wide variety of measurements suggest that a strength expressed by a coefficient of friction $\mu = 0.6$ to 1 and no cohesion is generally applicable to the earth's crust (known as Byerlee's law, Byerlee, 1978) when considering significant depths (see Zoback et al., 2003 for discussion), i.e. when the in-situ stresses are relatively large compared to the cohesion. For our case this assumption is probably valid below 400 mBGS ($S_v > 10$ MPa), but but has been shown to be invalid at shallow depth (i.e. with normal stress <5MPa) by Byerlee (1978, Fig. 3). Assuming that the shear strength of faults is dominated by friction, it is possible to constrain the maximum stress ratio using the following relation:

$$\sigma_1/\sigma_3 = (S_1 - P_p)/(S_3 - P_p) = [(\mu^2 + 1)^{1/2} + \mu]^2 \tag{3}$$

where:

σ_1 = maximum effective principal stress

σ_3 = minimum effective principal stress

S_1 = maximum total principal stress

S_3 = minimum total principal stress

P_p = pore pressure

μ = coefficient of friction

In a S_{Hmax} vs. S_{hmin} plot (see Figure 11 to Figure 14) this relation defines a polygon (thick black line) including all acceptable stress states.

Further constraints can be placed by evaluating the condition leading to no borehole failure. The maximum effective hoop stress, potentially leading to breakout formation, is given for a vertical hole by the following relation:

$$\sigma_{\theta\theta}{}^{max} = 3S_{Hmax} - S_{hmin} - P_p - \alpha P_p \qquad (4)$$

where:

$\sigma_{\theta\theta}{}^{max}$ = maximum tangential effective stress

S_{Hmax} = maximum horizontal stress (total stress)

S_{hmin} = minimum horizontal stress (total stress)

P_p = pore pressure

α = effective stress law coefficient for compressive failure

The first pore pressure term accounts for a borehole filled with water and the second pore pressure term comes from the effective stress law for compressive failure. No pressure (e.g. heavy drill mud) or temperature (cooling of the borehole during drilling) perturbations are considered in our analysis. Both the cooling of the drill hole and the use of heavy mud would tend to inhibit breakout formation and, if these terms are subsequently found to be significant, the stress analysis should be revisited. The effective stress law coefficient for compressive failure is usually considered to be equal to one, which is supported by laboratory results, even for low porosity rocks (Brace and Martin, 1968).

The maximum effective hoop stress given in equation (4) is computed for all possible couples of S_{hmin} and S_{Hmax} and contoured in Figures 11b, 12b, 13b and 14b. Knowledge of the borehole strength will then permit bounding of the horizontal stress magnitude. To get a good approximation of the borehole strength is not trivial. Common practice usually considers the borehole strength being represented by the UCS (e.g. Zoback et al., 2003). The main simplification of this approach is to consider that the borehole wall is loaded under uniaxial conditions, whereas the conditions are actually triaxial with some lateral confinement leading potentially to an increased apparent strength. Other effects like size effect, core damage, complex stress path, time-dependant behavior and strength degradation will affect borehole strength. In the current state of knowledge, it is not possible to balance the various effects in order to derive effective borehole wall strength. Various laboratory and field studies (e.g. Martin, 1997) have shown that the apparent strength of a borehole with a diameter larger than 100 mm could be slightly lower than the UCS. For larger excavations in massive to moderately jointed rocks, stress-induced failure (spalling) was shown to take place when the stress at the boundary of the excavation exceeded the crack initiation threshold, i.e. 0.3 to 0.5 UCS (e.g. Diederichs, 2007). For small openings (boreholes) under a true triaxial stress state, other studies (e.g., Mitri and Bétournay, 2006) suggest that borehole strength can be 1.5 to 2.0 times higher than UCS. The consequences of this uncertainty on the stress constraints are the following:

- *if UCS overestimates borehole wall strength:* our stress constraints will be too conservative, i.e. stress level will be lower than our proposed maximal horizontal stress magnitude.

- *if UCS underestimates borehole wall strength:* our stress constraints will be too restrictive, i.e. stress level could be higher than our proposed maximal horizontal stress magnitude.

Also we will consider the actual strength distribution (probabilistic approach) as determined in Section 3.3.1. Examples of the analysis are presented in Figures 11, 12, 13 and 14. The left frame of the figure shows the strength distribution at a given depth (log-normal distribution). As no failure was observed the stresses at the borehole wall have to be less than the left tail of the distribution. Assuming a 1% level being characteristic of no failure observation at the borehole wall, we can constrain the maximum allowable maximum horizontal stress. For example at 480 mBGS in the Queenston Formation (Figure 11), considering a 1% failure threshold, the maximum horizontal stress cannot exceed 17.5 MPa (red circle on Figure 11b). If the maximum horizontal stress was reaching 25 MPa (blue circle on Figure 11b), one should expect to see 20% of the borehole failing. Another example (at 680 mBGS in the Cobourg Formation) is presented in Figure 12. Following the same logic

INTERA

(<1% failure), we can constrain the maximum horizontal stress to be less than 30 MPa. Within lithology with relatively high strength (example at 370 mBGS in Salina A0 Unit in Figure 13), the absence of failure does not provide additional constraints on allowable stresses. Within weak rocks (example at 270 mBGS in the Salina B Unit in Figure 14), even at low stress levels, significant failure (>20%) is expected.

The analysis was repeated for every depth and the results are summarized in Figure 15. The 1% threshold (basically no failure) is represented by a green line. In summary, the constraints for the maximum horizontal stress are the following:

1) for 0 to 150 mBGS: no additional constraints on stress.

2) for 150 to 300 mBGS: within very weak rock, failure is expected. Washout are observed and they may well mask and be partially due to stress-induced failure. Due to this uncertainty, we have poor control on stress level for this section.

3) for 300 to 340 mBGS, maximum horizontal stress is $1.5S_v$ or less.

4) for 340 to 420 mBGS, within very strong rock the absence of failure provides poor constraints on stress.

5) for 420 to 520 mBGS, maximum horizontal stress is 1.0 to $1.5S_v$ or less.

6) for 520 to 650 mBGS, fairly weak rock but no failure observed. To be in agreement with the observations, the stress has to be low, probably not more than $0.75S_v$.

7) for 650 to 740 mBGS variable strength, maximum horizontal stress could be as high as $2.3S_v$ for the stronger rocks, but no more than $0.75S_v$ for the weaker rocks.

If the strength of the borehole wall is actually 1.5 UCS, as suggested in some recent publications (e.g., Mitri and Bétournay, 2006), the stress constraints based on a 1% failure probability will be less restrictive and would approximately follow the 20% failure line on Figure 15 (computed fro a strength of 1.0 UCS. A summary of the constraints on horizontal stresses at 680 mBGS, for the various borehole wall strength scenarios discussed above, are listed in Table 2.

Table 2   Constraints on the Horizontal Stress Magnitude at a depth of 680 mBGS, Assuming Various Scenarios for the Borehole Wall Strength. Log Normal Parameters Describe the Best Fitted Log Normal Distribution over the Lab Strength Measurement Results. Vertical stress at 680 mBGS Depth is about 18 MPa

Borehole Wall Strength Estimated by:	Mean strength [MPa]	Log normal parameters		Bounds on horizontal stress magnitude [MPa]		Maximum S_{hmax}/S_{hmin} Ratio	Maximum S_{hmax}/S_v Ratio
1.5 UCS	161	5.0329	0.341	9	42	4.67	2.33
UCS	107	4.6275	0.341	9	30	3.33	1.67
0.75UCS	80	4.3398	0.341	9	24	2.67	1.33
0.5UCS	54	3.9343	0.341	9	18	2.00	1.00
0.3UCS	32	3.4235	0.341	9	14	1.56	0.78

4   Review of Stress Data Base for Southern Ontario

Three stress databases for the Great Lakes area have been collected:

1) The stress database from the World Stress Map project version 2008 (Heidbach et al., 2008)

2) A stress data compilation from Adams (1995)

3) A stress data compilation presented in Maloney et al. (2006)

Figure 16a shows the stress orientations from WSM2008 and Adams data. Figure 16b solely presents the WSM2008 database and captures only the higher trends (1st order stress province (Zoback, 1992)). The combined data presented in Figure 16a indicates that the Adams database shows a large scatter in stress orientation which is probably representative of actual stress heterogeneities and variability within the earth's crust.   For the area of interest, the high order trend for the maximum horizontal stress is NE-SW.

Stress magnitudes vs. depth are presented in Figures 17 and 18. The following information can be derived from these figures:

- The data support the assumption that below 400 mBGS, that Byerlee's law is valid.

- The data shows that close to surface, the horizontal stress magnitude is usually higher than 0 MPa (0 – 10 MPa for S_{hmin} and 0 – 20 MPa for S_{Hmax}). Thus for shallow depth, Byerlee's law is too restrictive.

- The data span is in general agreement with the constraints derived in our study.

5   Discussion

No typical stress-induced borehole failure was observed in the acoustic borehole images of DGR-1, DGR-2, DGR-3 and DGR-4. However, a detailed analysis of the transit time log indicated borehole enlargement at depths where the rock mass is weak. The shape analysis of borehole sections shows that the elongation of the borehole is usually small (less than 5%) and that the orientation of the elongation is usually random. There is one exception to it, in the Ordovician argillaceous limestones of the Cobourg, Sherman Fall and Kirkfield Formations, where a systematic SE major ellipse axis orientation is found (see Figure 6). Comparing this preferential orientation with the borehole trajectory allows exclusion of the influence of the repeated wearing of the borehole walls by the drill string as an explanation of this preferential orientation. While there is no definitive explanation concerning the mechanism leading to this borehole elongation, interpretation of it in the classical breakouts interpretation way, indicates a S_{Hmax} oriented NE–SW. This result is in agreement with the regional stress orientations presented in Figure 16a and Figure 16b.

Concerning stress magnitudes, the analysis was based on the observation of the absence of wellbore failure and back calculation of what the possible stress state would be to correspond with these observations. Two additional assumptions were also made:

- the strength of the crust is driven by the shear strength of optimally oriented fractures with a coefficient of friction of 1.0 and no cohesion.

- the strength of the borehole wall was assessed probabilistically and was assumed to be properly represented by the ultimate strength of core samples loaded under uniaxial stress conditions (UCS).

The first assumption is generally accepted at sufficient depth, where cohesion becomes negligible in comparison to the stress levels. However, for shallow depth (<400 m), this assumption is not valid (see stress database in

Figure 17).

The constraints on horizontal stress derived in this study, displayed in Figure 15 and summarized in Section 3.3.2 suggest that the stress profile may show a layered structuring, with stress riser horizons and other layers showing lower stress levels. Such structuring could be explained by the stiffness contrast between the layers (see Figure 9), the stiff layers acting like back bones and attracting stresses. In order to test this hypothesis, a 2D finite element model was built reproducing the stiffness variability measured on core samples (Figure 19). The software used was Phase^2 (Rocscience, 2005). The model built is a square with a side size of 1000 m. Constrained displacement boundary (rollers) were set at the lower and most left end of the model. The upper end is a free boundary. A fixed displacement boundary condition was applied to the right end of the model in order to simulate tectonic loading. The initial conditions include lithostatic vertical stress initialization, but no horizontal stress or out of plane stresses. The model was solved in plane strain for purely linear elastic materials. Screenshots of the mesh and the model output are presented in Figure 20. The model shows clean results without boundary effect and with a homogenous displacement field.

The magnitude of the displacement at the fixed displacement boundary was adjusted to obtain a proper fit with the stress constraints derived from the absence of borehole failure. A displacement of 0.7 m (a strain of 0.07%) produced a reasonable fit (see Figure 21).

These results do not provide constraints on stress magnitude per se because we have no control on what was the actual strain applied in the tectonic history of the area. Also the intact rock stiffness obtained on small size core samples was used in the model. The rock mass stiffness (at large scale) will be generally less than that of the intact rock. For a rock mass with a GSI (Geological Strength Index) of 50, the rock mass moduli will be only about 30% of the intact rock moduli (Hoek and Diederichs, 2006). In order to get similar fit to the data, the strain will need to be multiplied by 3 and will be about 0.2% which is still a plausible value. It is also to be expected that some de-confinement occurs close to surface due to the effect of structures (Maloney et al., 2006) which will reduce the maximum horizontal stress at surface to value more realistic than the one provided by the model output (10 to 20 MPa instead of 37 MPa). The important information from this modeling exercise is that it provides a qualitative indication that the stiffness contrast between the different formations could be a prominent factor in the variability and distribution of stress at the Bruce site.

6   Conclusions

The suite of logs run in boreholes DGR-1, DGR-2, DGR-3 and DGR-4, particularly the acoustic borehole image logs, were analyzed for indications of stress-induced wellbore failure which could assist in estimating the possible stress state at the Bruce site. No wellbore failures were observed, but a systematic SE elongation of a restricted section was highlighted by the borehole section shape analysis. Interpretation of this elongation in the classical breakout analysis way implies a NE-SW maximum horizontal stress direction.

The absence of stress-induced wellbore failures does not provide a strong constraint on the possible stress state, both orientation and magnitude. Consequently, the level of confidence in the stress characterization derived here remains relatively low. To improve upon the stress characterization described here, other stress measurement techniques will need to be applied. However, the current stress analyses provide the best available constraints on in-situ stress magnitudes at the Bruce site (see Section 3.3.2). The absence of borehole breakouts permits setting of an *upper bound* on the allowable maximum horizontal stress magnitude. Variation of constraints with depth and numerical modeling suggest that the stiffness contrasts between the different stratigraphic units may be playing a significant role in controlling the ground stress distribution with depth.

7   References

Adams, J., 1995. The Canadian Crustal Stress Database - a Compilation to 1994. GSC Open File #1622.

Bell, J.S. and D.I. Gough, 1979. Northeast-southwest compressive stress in Alberta: Evidence from oil wells, Earth and Planetary Science Letters, Vol. 45, pp. 475-482.

Brace, W.F. and R.J. Martin, 1968. A test of the law of effective stress for crystalline rock of low porosity, International Journal of Rock Mechanics and Mining Science, Vol. 5, pp. 415-426.

Brudy, M. and M.D. Zoback, 1999. Drilling -induced tensile wall-fractures: Implications for determination of in-situ stress orientation and magnitude, International Journal of Rock Mechanics and Mining Science, Vol. 36, pp. 191-215.

Byerlee, J., 1978. Friction of Rocks, Pure and Applied Geophysics, Vol. 116, pp. 615-626.

Deere, D.U., 1968. 1 Geological Consideration in Rock Mechanics in Engineering Practice, eds. K. G. Stagg and O.C. Zienkiewicz, John Wiley & Sons.

Diederichs, M.S., 2007. The 2003 Canadian Geotechnical Colloquium: Mechanistic interpretation and practical application of damage and spalling prediction criteria for deep tunneling, Canadian Geotechnical Journal, Vol. 44, pp.1082-1116.

Grubbs, F.E., 1969. Procedures for Detecting Outlying Observations in Samples, Technometrics, Vol. 11, pp.1-21.

Halíř, R. and J. Flusser, 1998. Numerically Stable Direct Least Squares Fitting of Ellipses. in Proc. Int. Conf. in Central Europe on Computer Graphics, Visualization and Interactive Digital Media, pp. 125-132, ed. V. Skala.

Heidbach, O., M. Tingay, A. Barth, J. Reinecker, D. Kurfeß and B. Müller, 2008. The 2008 release of the World Stress Map (available online at www.world-stress-map.org).

Hoek, E. & M.S. Diederichs, 2006. Empirical estimation of rock mass modulus, International Journal of Rock Mechanics and Mining Sciences, Vol. 43, pp. 203-215.

Intera Engineering Ltd., 2009a. Technical Report: Analyses of DGR-1 and DGR-2 Borehole Images for Stress Characterization, TR-08-04, Revision 0, March 10, Ottawa.

Intera Engineering Ltd., 2009b. Technical Report: Laboratory Geomechanical Strength Testing of DGR-1 & DGR-2 Core, TR-07-03, Revision 3, February 3, Ottawa.

Intera Engineering Ltd., 2009c. Technical Report: Long-Term Strength Degradation Testing of DGR-2 Core, TR-08-11, Revision 0, June 16, Ottawa.

Intera Engineering Ltd., 2009d. Technical Report: Laboratory Geomechanical Strength Testing of DGR-3 and DGR-4, TR-08-24, Revision 0, November 12, Ottawa.

Intera Engineering Ltd., 2006. Geoscientific Site Characterization Plan, OPG's Deep Geologic Repository for Low and Intermediate Level Waste, Report INTERA 05-220-1, OPG 00216-REP-03902-00002-R00, April, Ottawa.

Maloney, S., P.K Kaiser and A. Vorauer, 2006. A Re-assessment of In-situ Stresses in the Canadian Shield. in Golden Rocks 2006, The 41st U.S. Symposium on Rock Mechanics (USRMS), Golden, Colorado.

Martin, C.D., 1997. Seventeenth Canadian Geotechnical Colloquium: The effect of cohesion loss and stress path on brittle rock strength, Canadian Geotechnical Journal, Vol. 34, pp. 698-725.

Mitri, H.S. and M.C. Bétournay, 2006. Progressive failure of norite rock under biaxial loading conditions, CIM Bulletin, No. 99.

Rocsience Inc., 2005. Phase 2 version 6.0 - Finite Element Analysis for Excavations and Slopes. www.rockscience.com, Toronto, Ontario, Canada.

Zoback, M.D., C.A. Barton, M. Brudy, D.A. Castillo, T. Finkbeiner, B.R. Grollimund, D.B. Moos, P. Peska, C.D. Ward and D.J. Wiprut, 2003. Determination of stress orientation and magnitude in deep wells, International Journal of Rock Mechanics and Mining Sciences, Vol. 40, pp. 1049-1076.

Zoback, M.L., 1992. First- and second-order patterns of stress in the lithosphere: The World Stress Map Project, Journal of Geophysical Research, Vol. 97, pp. 11703-11728.

APPENDIX A

Figures 1 to 21
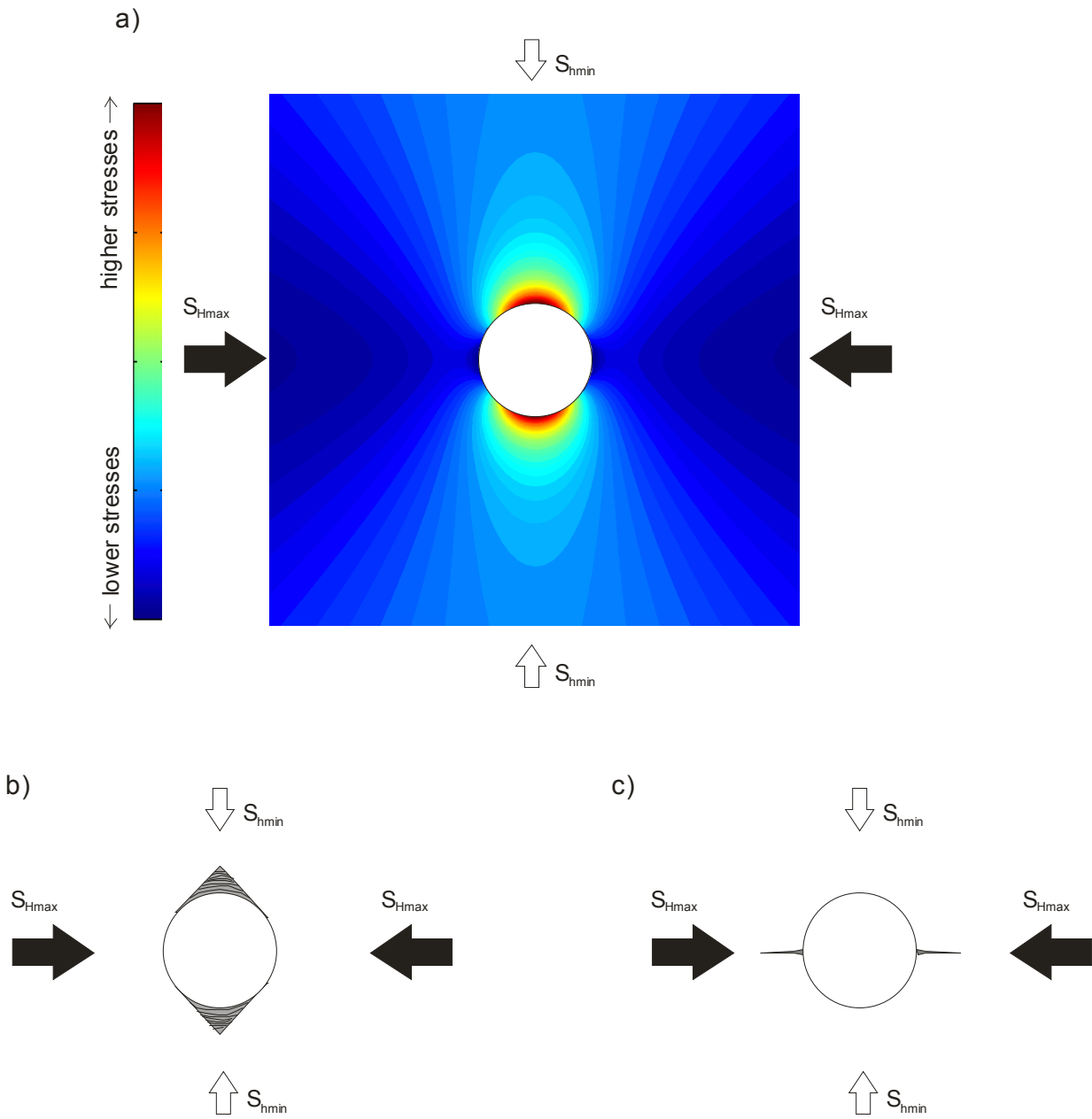
Figure 1   a) Stress concentration around a borehole. This stress concentration can be the cause of two type of stress-induced borehole wall failure: b) the breakouts in the compressive section of the borehole section or c) the drilling induced tension fractures (DITFs) in the less compressive and potentially tensile section of the borehole wall.
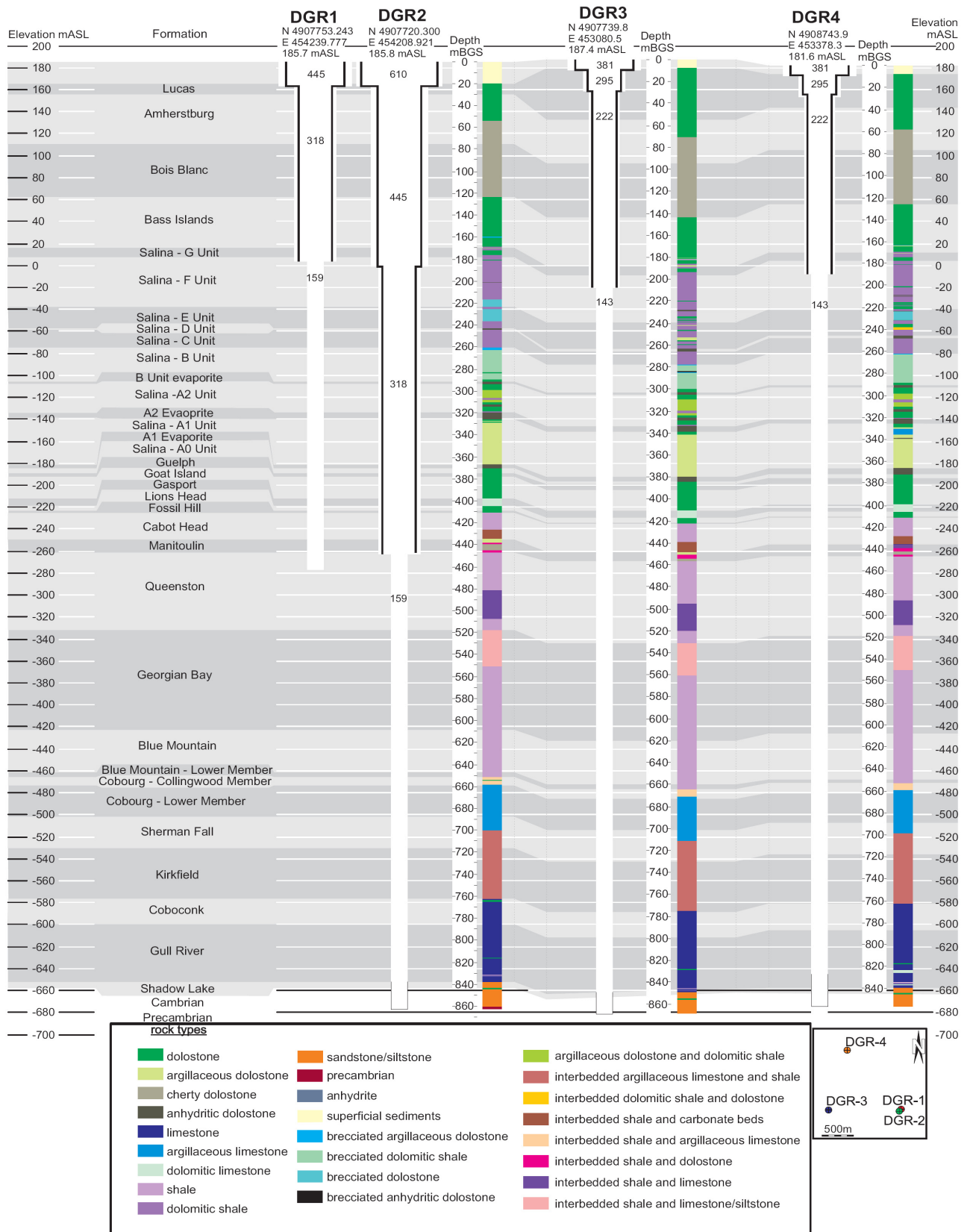
Figure 2   Borehole technical sections, formation correlation between wells and lithological column for each hole. The lower right frame presents the relative borehole collar positions in plan view.
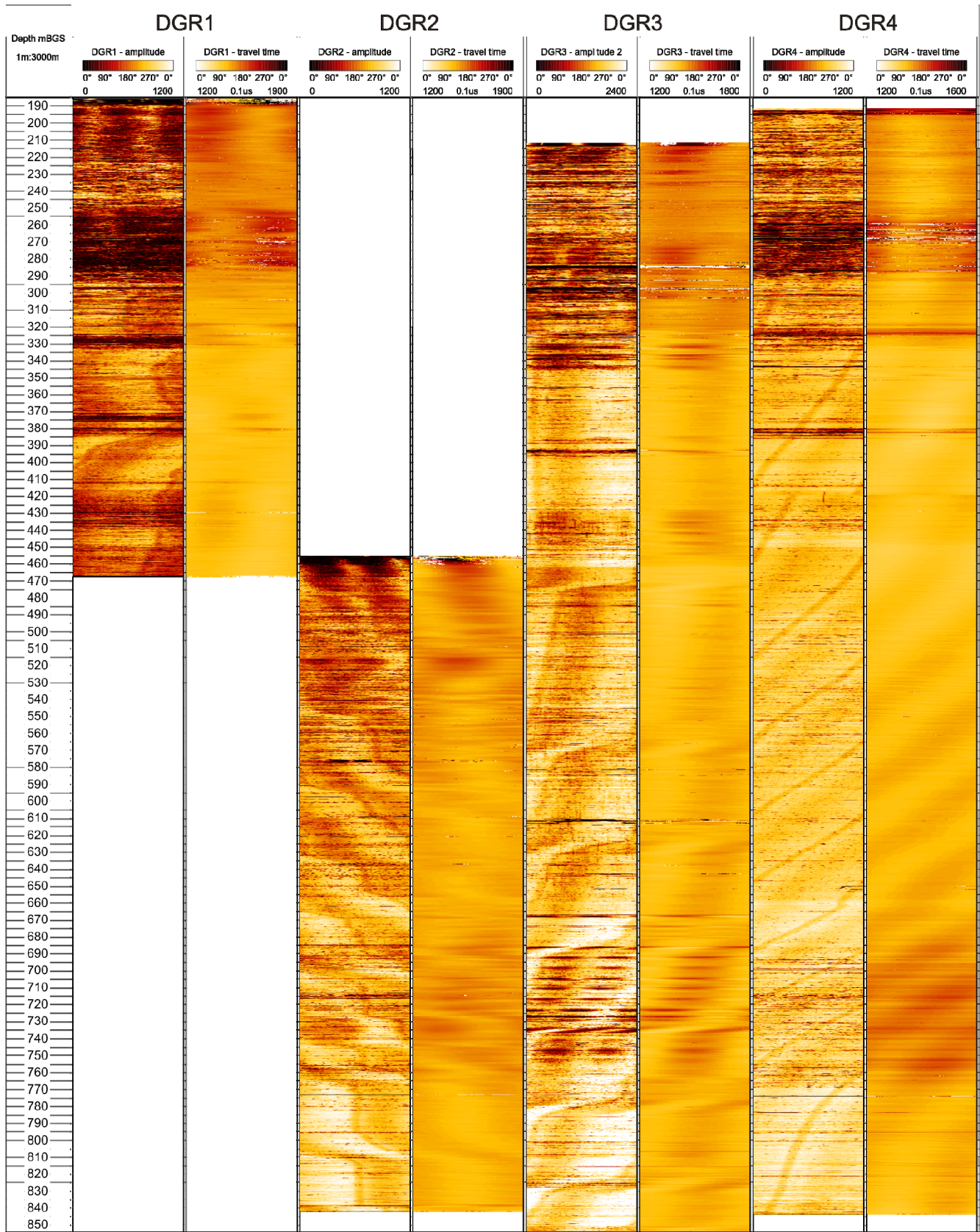
Figure 3   Display of the ABI images. Depth was not correlated.
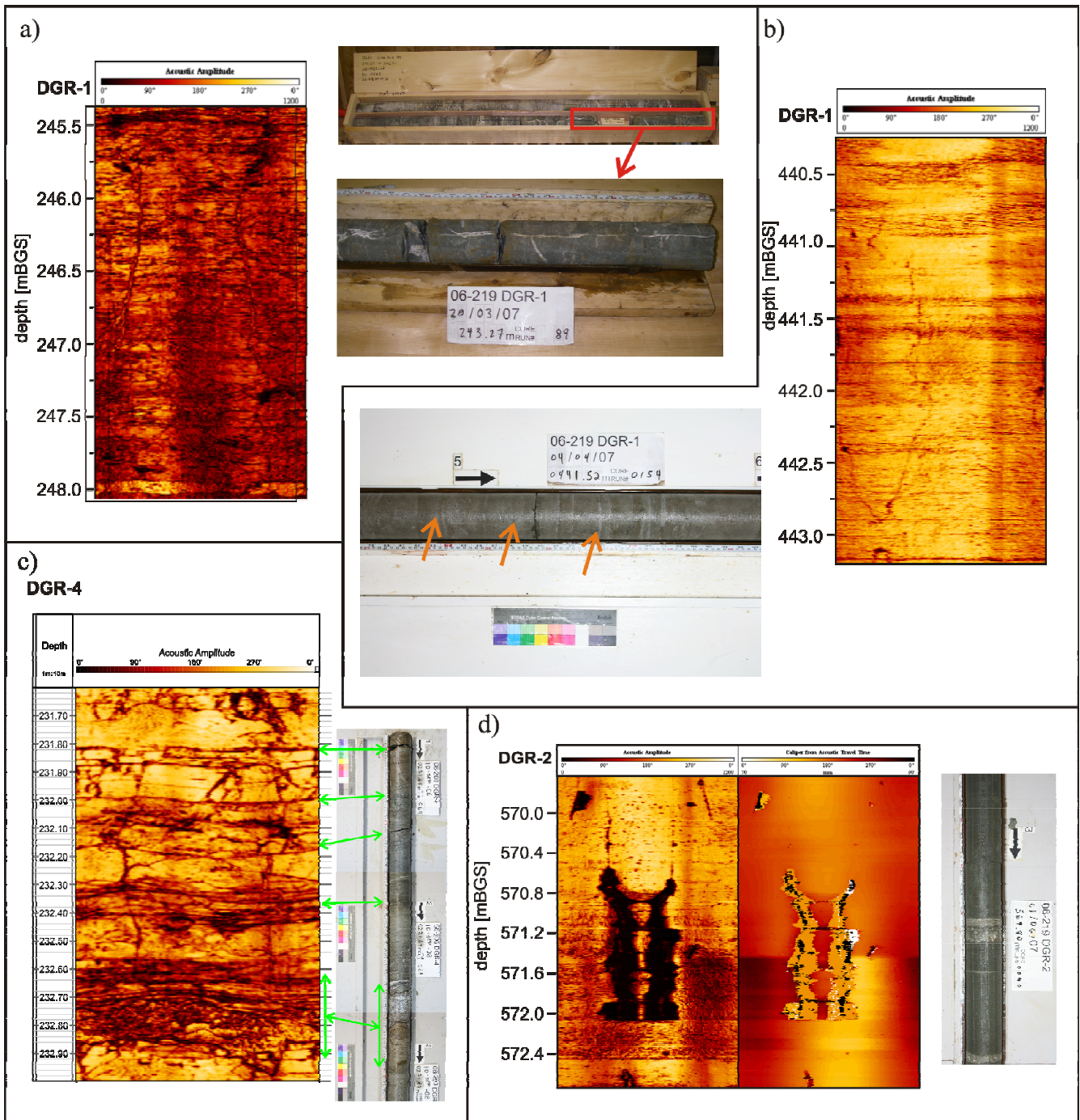
Figure 4   Example of potential stress-induced failure in the holes DGR-1, DGR-2, DGR-3 and DGR-4. After comparison with core photos, it is concluded that none of these feature are stress induced; they are related to pre-existing natural fractures.
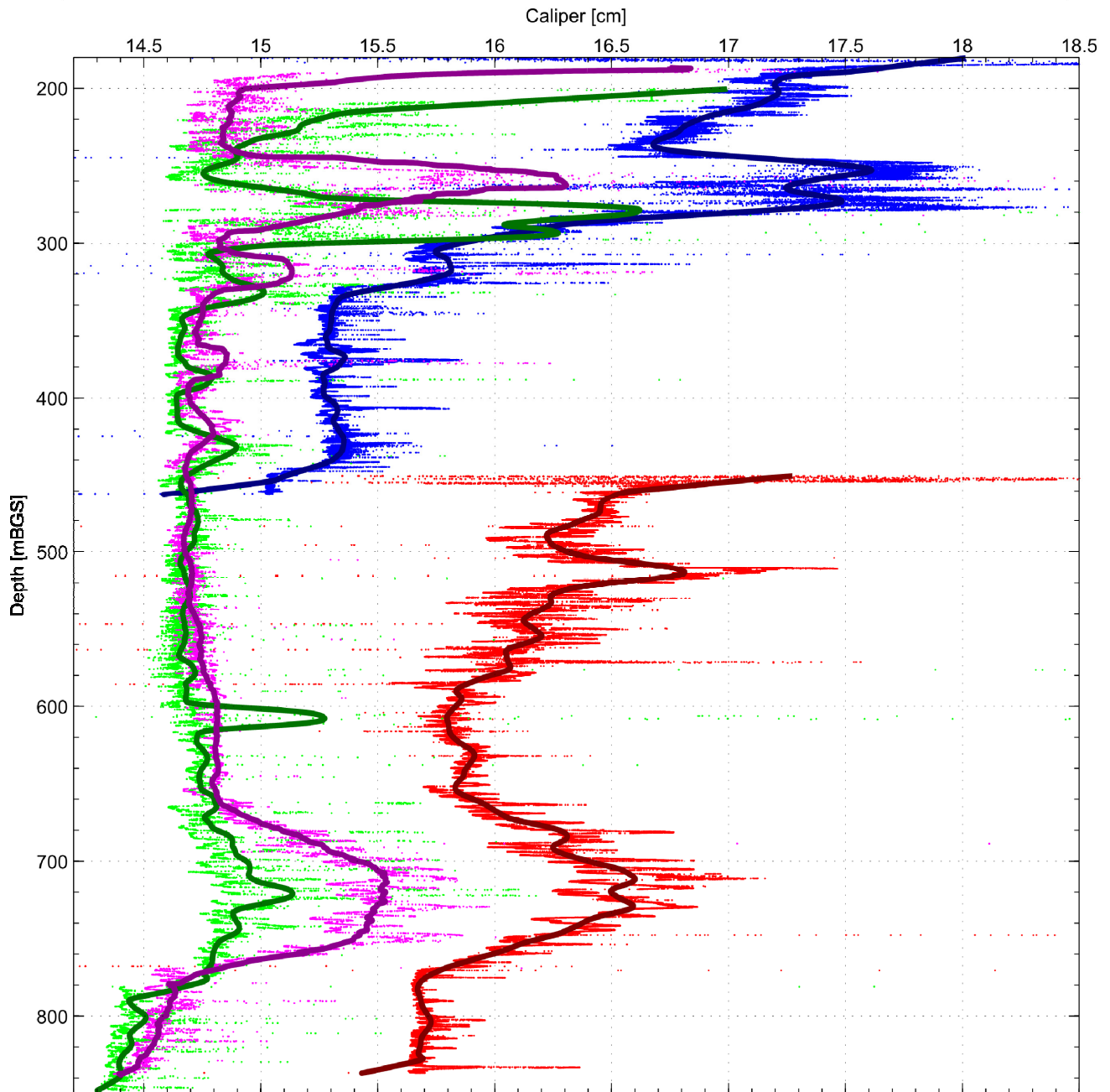
Figure 5   Caliper logs for DGR-1 (blue), DGR-2, (red) DGR-3 (green) and DGR-4 (magenta). For DGR-1 and DGR-2 these are mean borehole diameter derived from acoustic televiewer logs. For DGR-3 and DGR-4, 3-arm mechanical caliper logs are used to derive borehole diameter.   Dots are raw measurements and the lines represent smoothed data using a 20 m moving average filter.
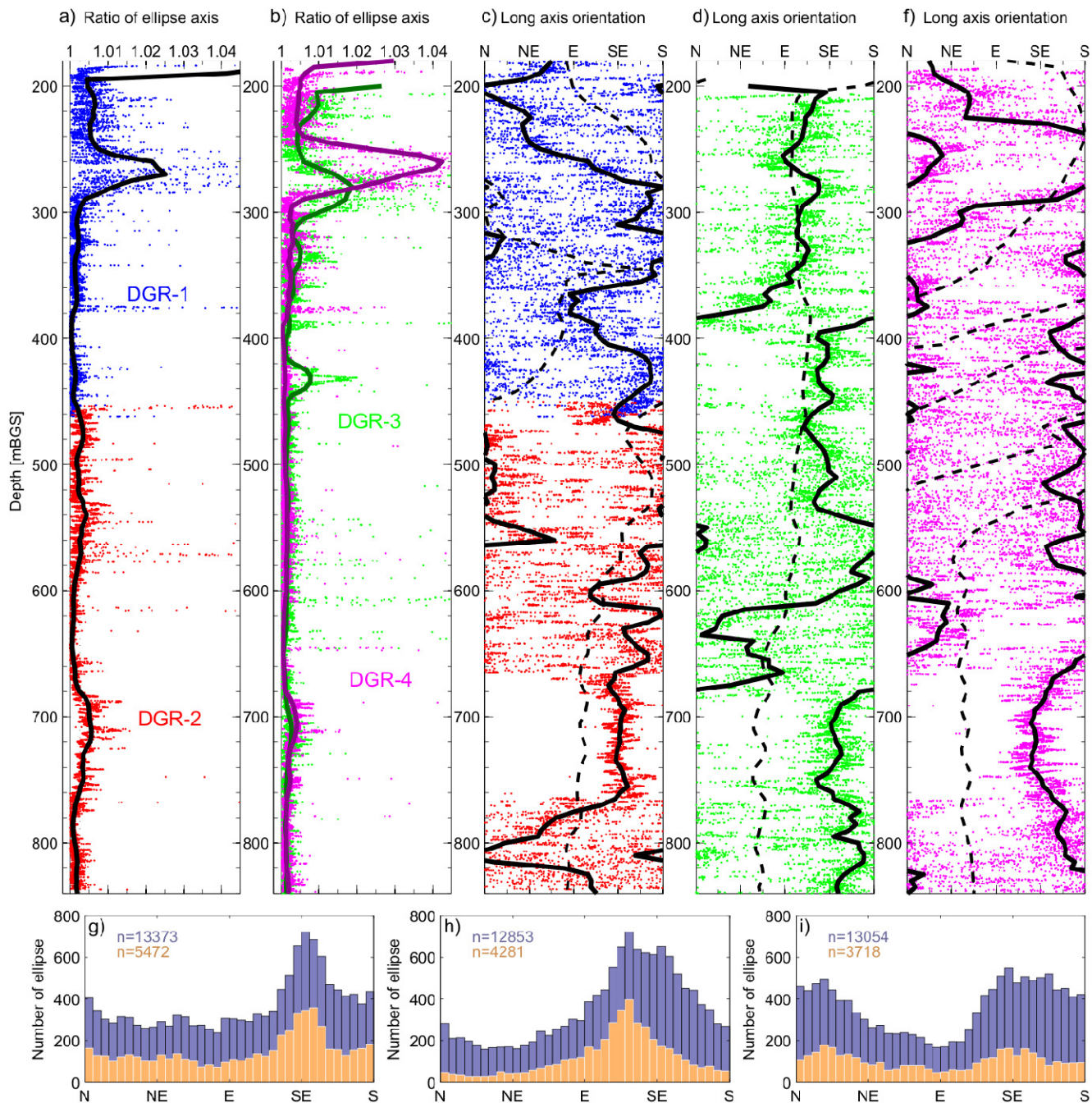
Figure 6   a) Ellipse axis ratio for DGR-1 (blue) and DGR-2 (red). The black line highlights the trend (20 m moving average filter). b) Ellipse axis ratio for DGR-3 (green) and DGR-4 (magenta) with 20 m moving average filters (thick lines) c) Ellipse orientation for DGR-1 and DGR-2. The thick black line highlights the trend using a 20 m moving average window. d) Ellipse orientation for DGR-3 d) Ellipse orientation for DGR-4. g) h) and i) Ellipse orientation histograms for DGR-1 and DGR-2, DGR-3 and DGR-4 respectively. In blue all orientations and in orange ellipses with axis ratio higher than 1.0025.
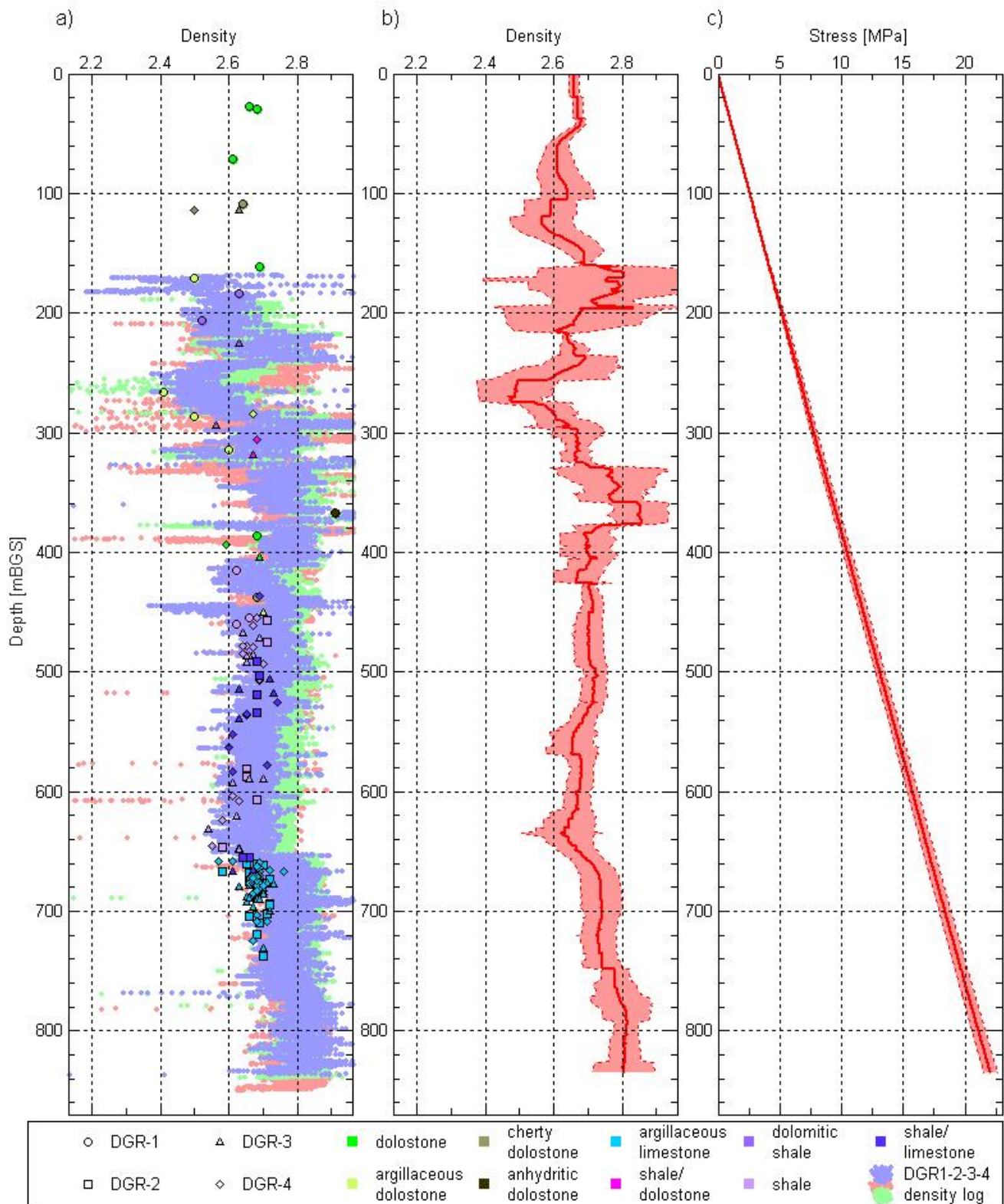
Figure 7 a) Compilation of lab and in-situ density data. Sample descriptions based on simplified lithologies from Figure 2. b) Mean density profile with standard deviation including both lab and in-situ measurements. c) Vertical stress profile derived by integration of the mean density profile. Best fit linear profile: S_v [MPa]=26.3*depth[km].
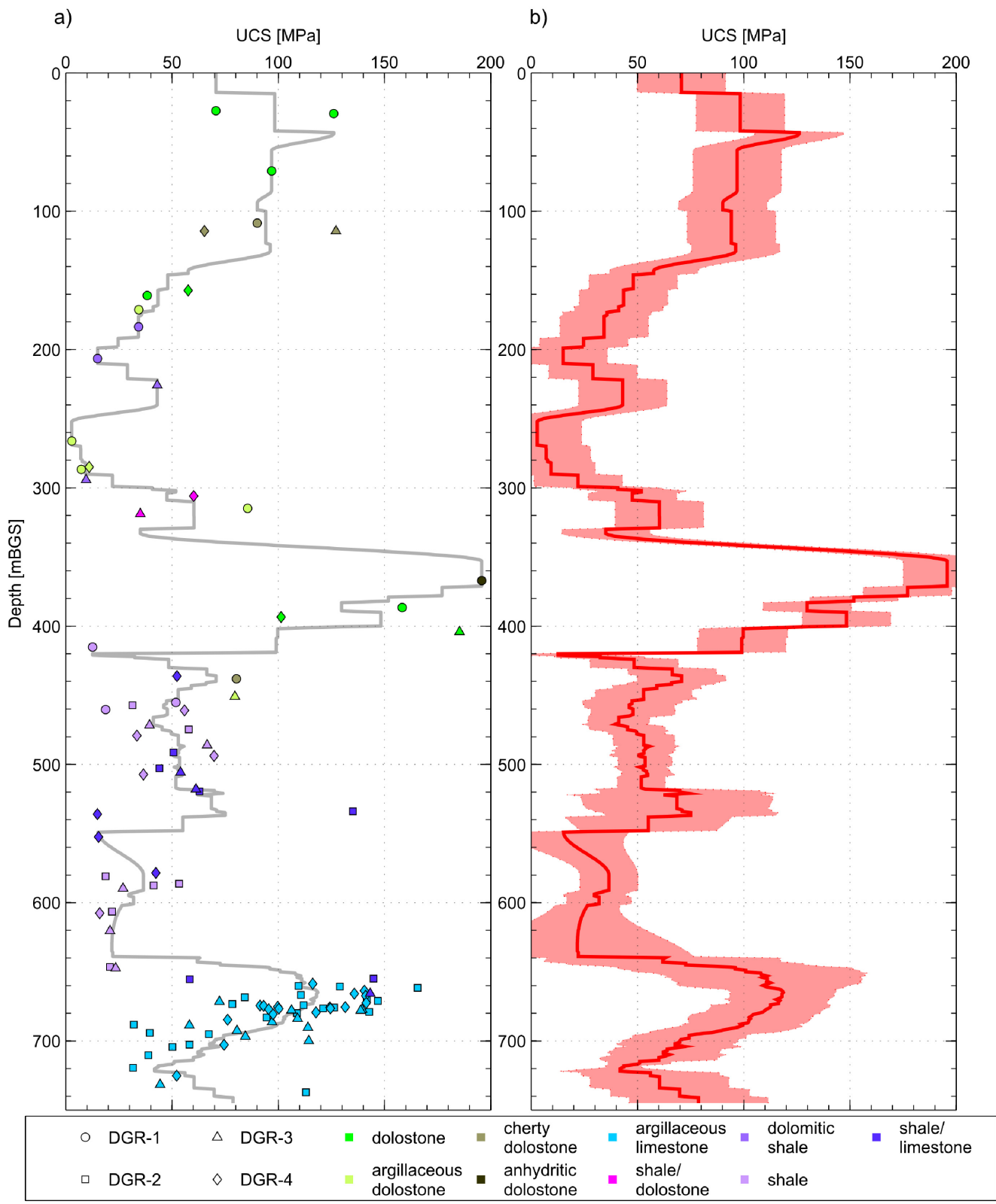
Figure 8 a) Compilation of lab UCS results. Sample descriptions based on simplified lithologies from Figure 2. The gray line is average interpolated UCS. b) Interpolated mean UCS with 1 standard deviation using a 30 m moving window.
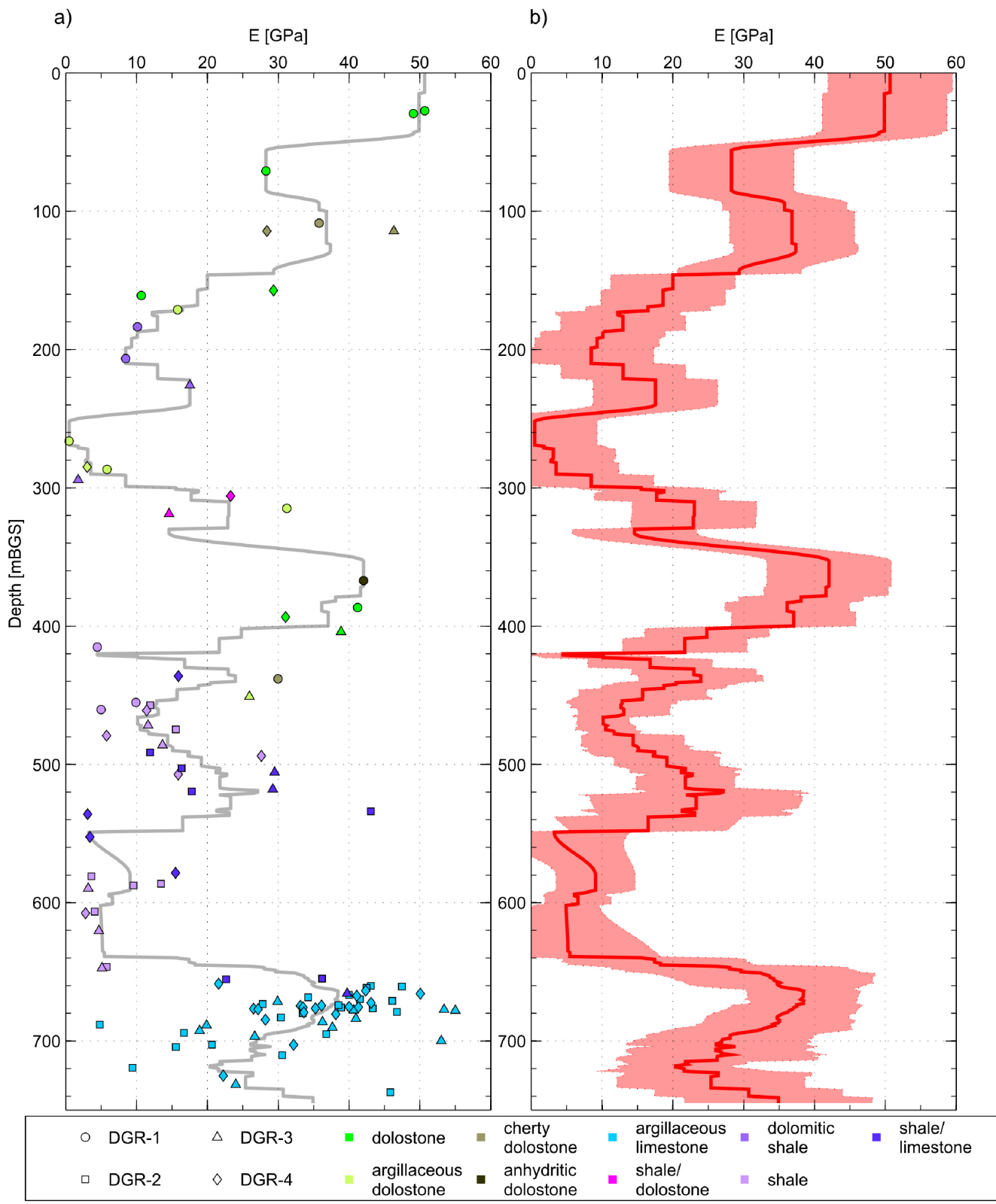
Figure 9   a) Compilation of lab E-modulus results. Sample descriptions based on simplified lithologies from Figure 2.   The gray line is mean interpolated E-modulus. b) Interpolated mean E-modulus with 1 standard deviation using a 30 m moving window.
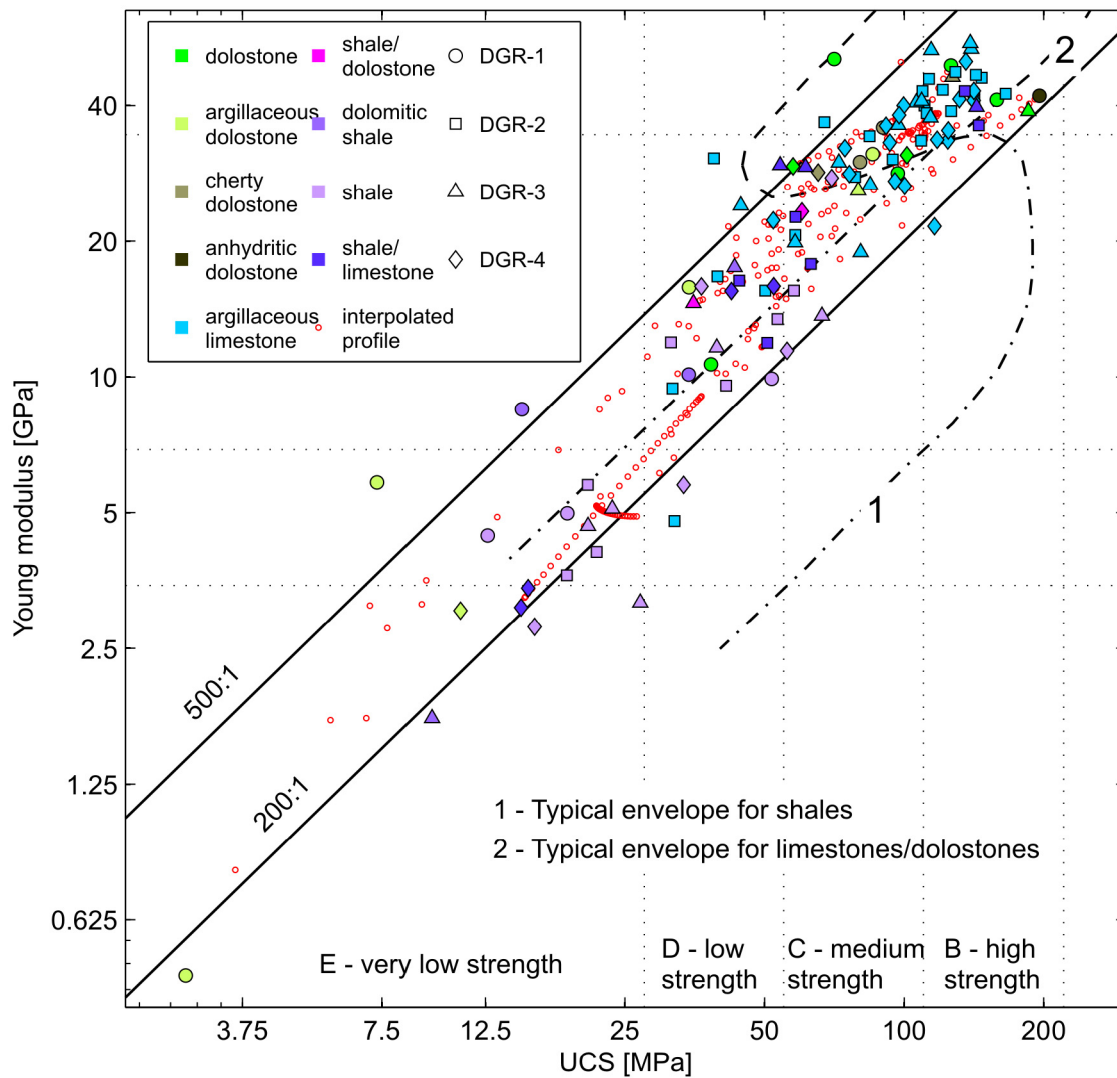
Figure 10   Young's Modulus vs. UCS plot following Deere (1968) rock classification approach. Sample descriptions based on simplified lithologies from Figure 2. Most of the results fit within expected strength/stiffness ratios for limestone/dolostone, shales or intermediate members.
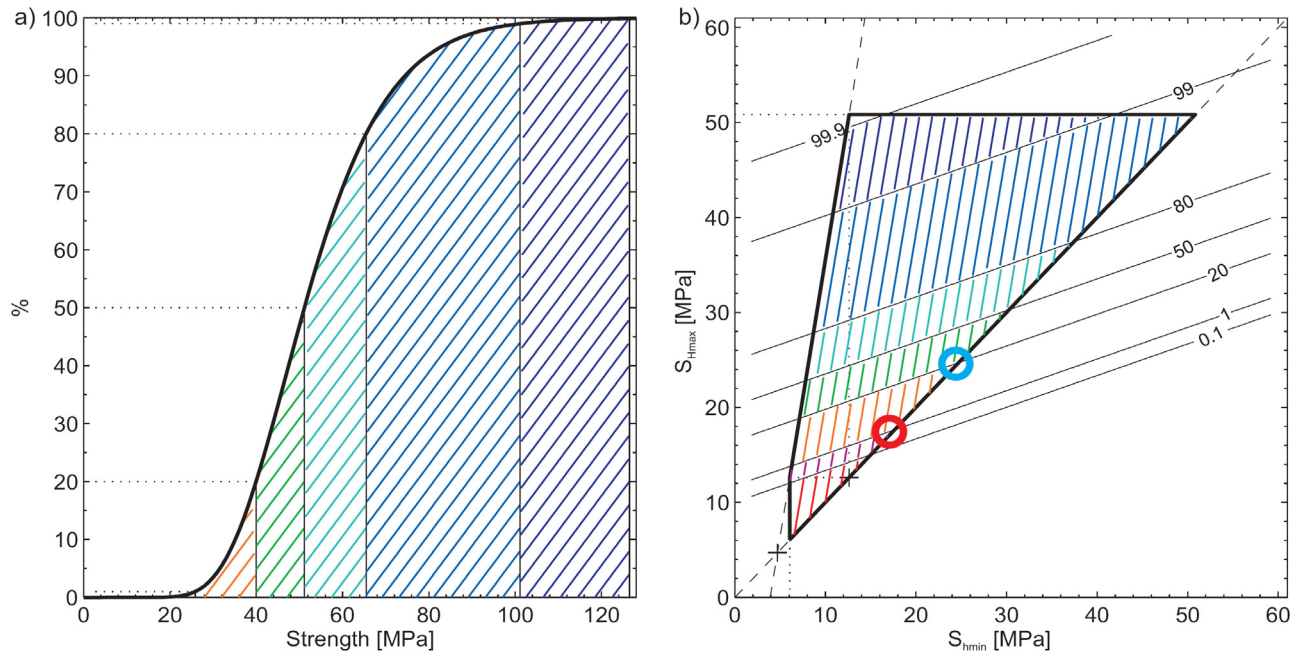
Figure 11   Stress analysis at 480 mBGS. The strength is estimated to be 53±14 MPa (mean ± std) and the best fit log normal parameters are 3.94 and 0.29. The corresponding log-normal cumulative strength distribution is presented in a) with coloured probability levels at 0.1%, 1% 20%, 50% 80%, 99% and 99.9%. The stress polygon in S_{hmin}-S_{Hmax} space for a coefficient of friction of 1 is plotted in black on b). The maximum stress levels at the borehole wall ($3S_{Hmax}$-S_{hmin}-$2P_p$) are contoured with labelling relative to equivalent probability. This means that in order to have less than 1% probability of failure of the borehole walls, the stress level must not exceed the 1% line.
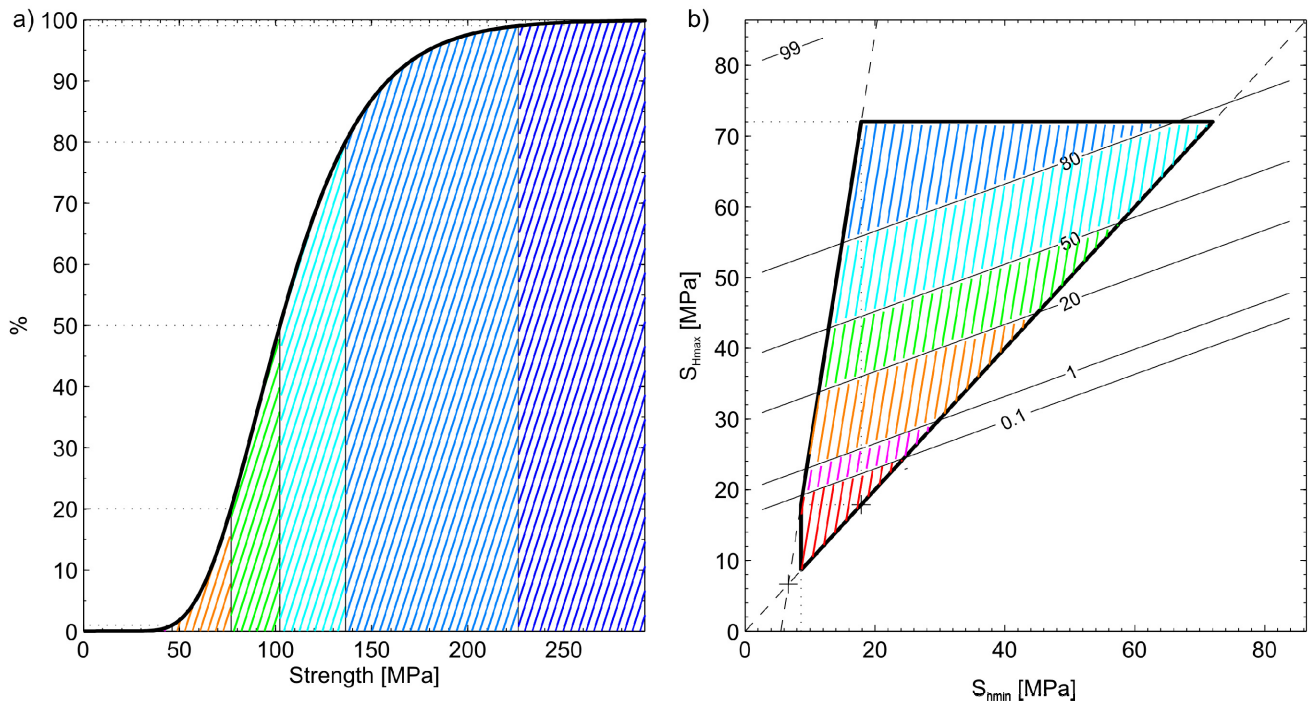
Figure 12   Idem to Figure 11 but at a depth of 680 mBGS (UCS=107±29 MPa, log-normal parameters are 4.63 and 0.34).
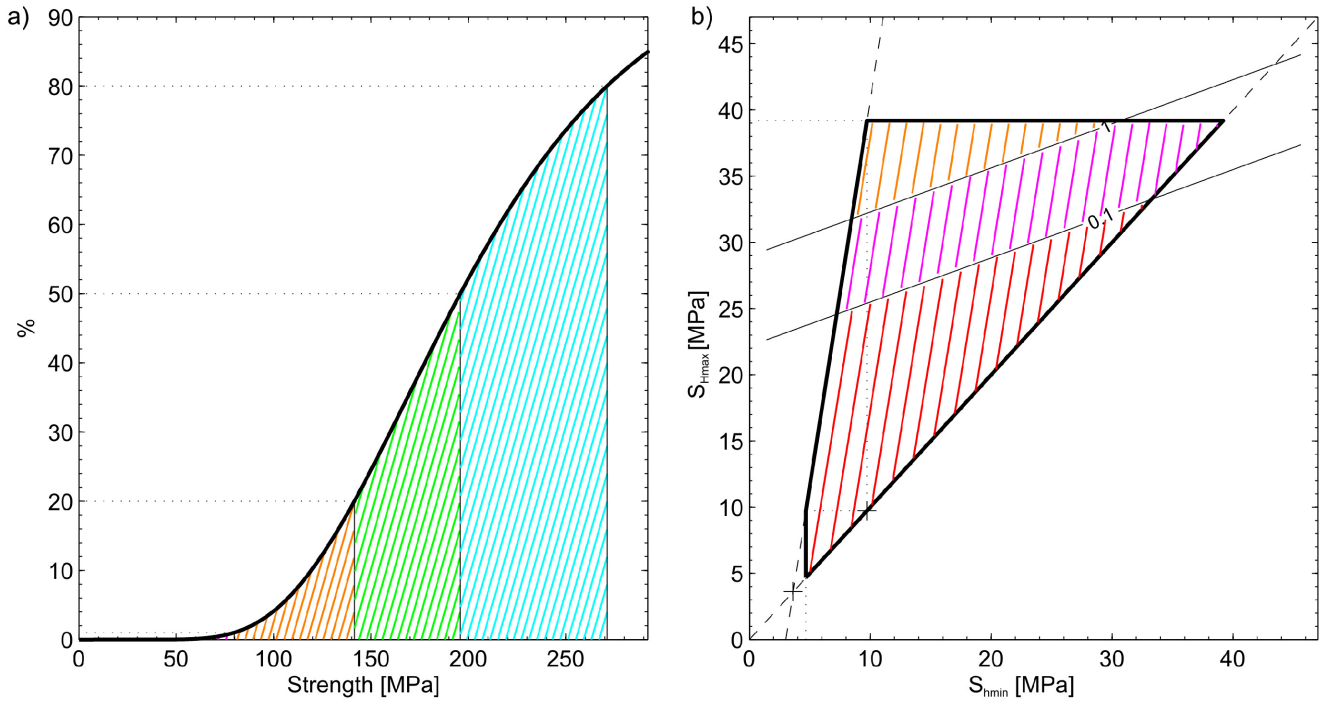
Figure 13   Idem to Figure 11 at a depth 370 mBGS. Here the strength estimate is very high: UCS=196±21 MPa (log-normal parameters are 5.28 and 0.39). In such situations, the absence of failure provides almost no additional constraint to the allowable maximum horizontal stress.
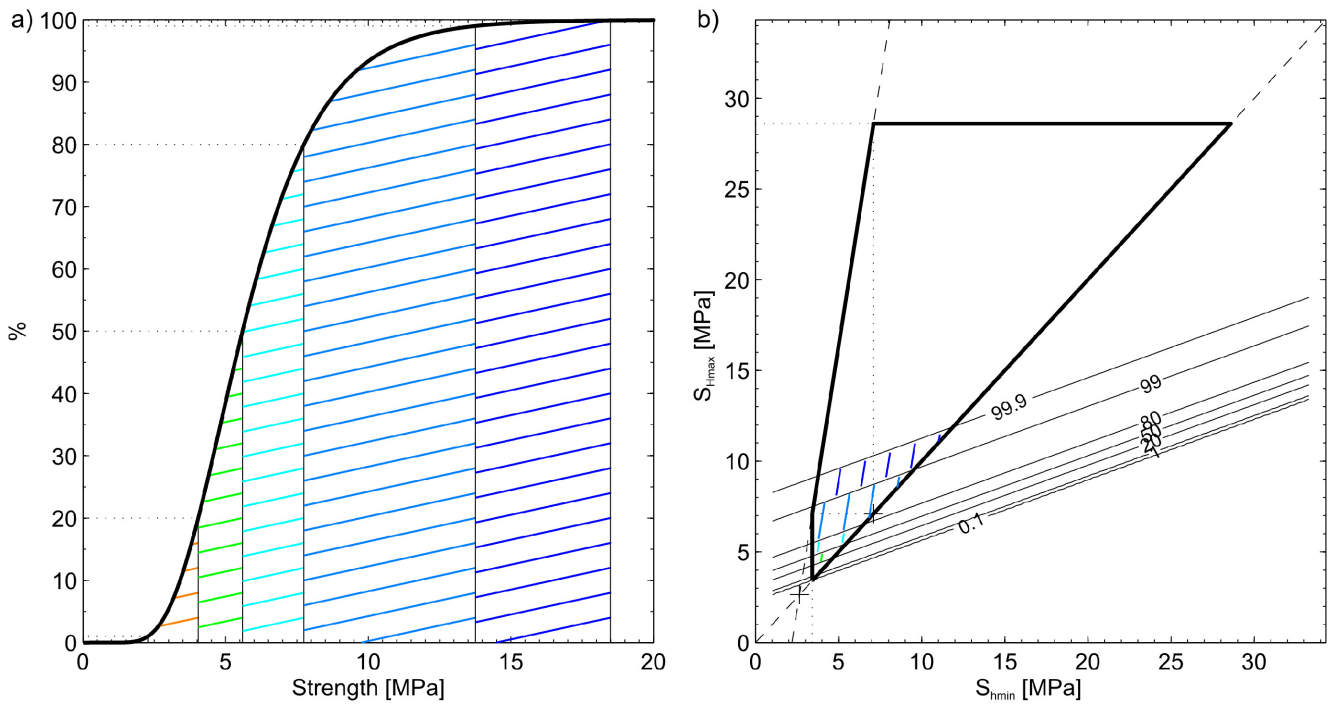
Figure 14   Idem to Figure 11 at a depth of 270 mBGS where the strength estimate is very low: UCS=7±21 MPa (log-normal parameters are 1.72 and 0.39). In such situations, even with low stress levels (at the bottom of the stress polygon) 50% or more of the borehole wall should show stress-induced failure.
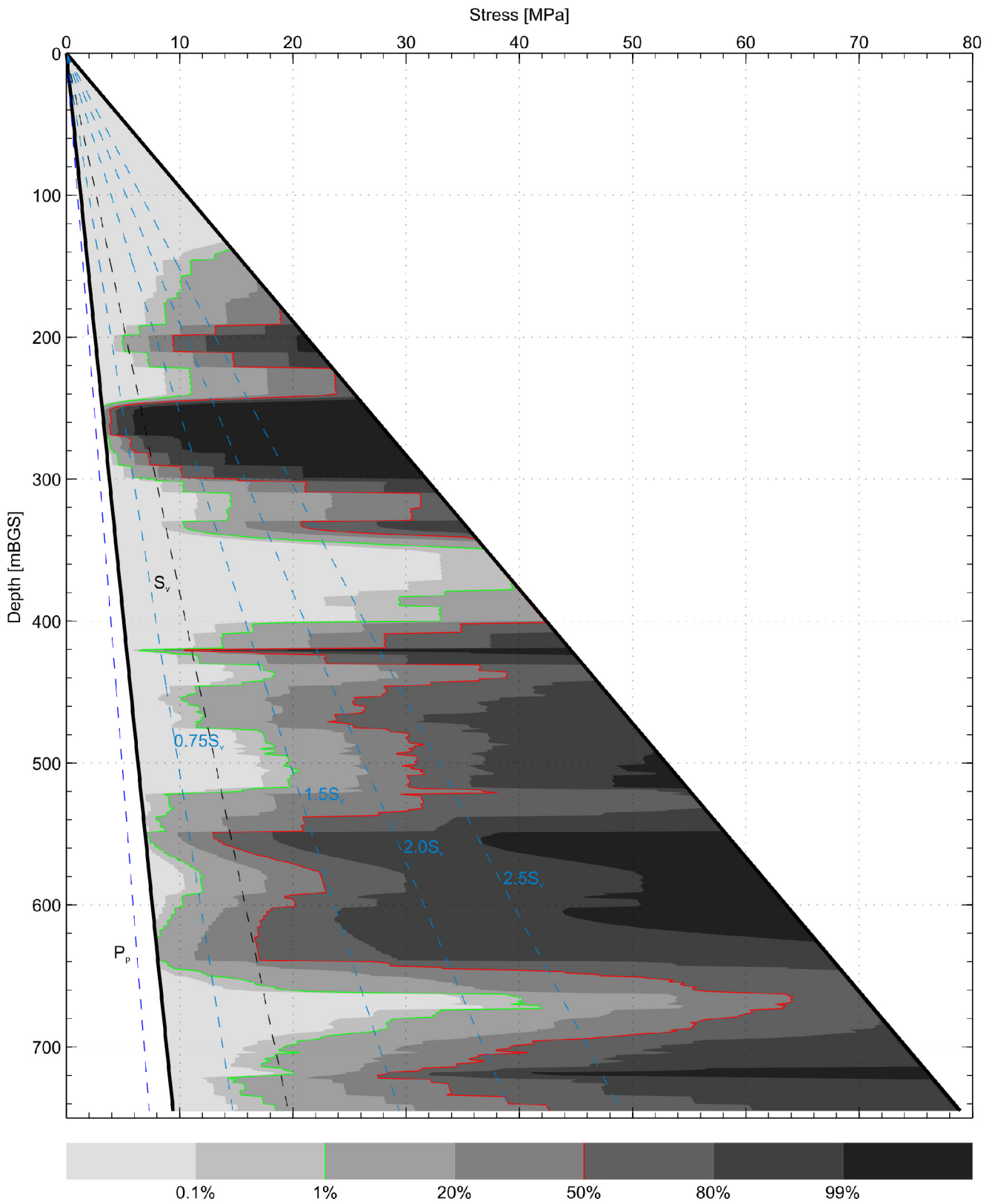
Figure 15   Summary of general constraints set on the maximum horizontal stress assuming borehole wall strength of 1.0 UCS. Horizontal axis is probability of borehole wall failure.
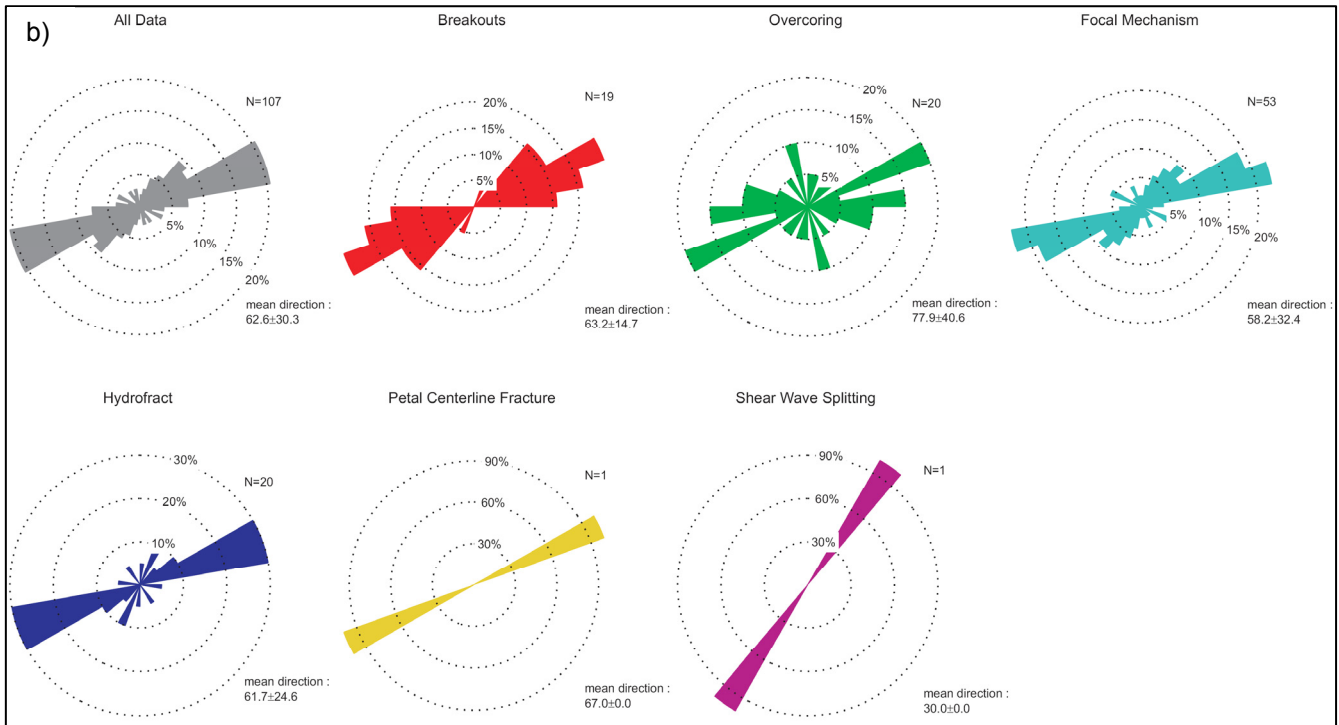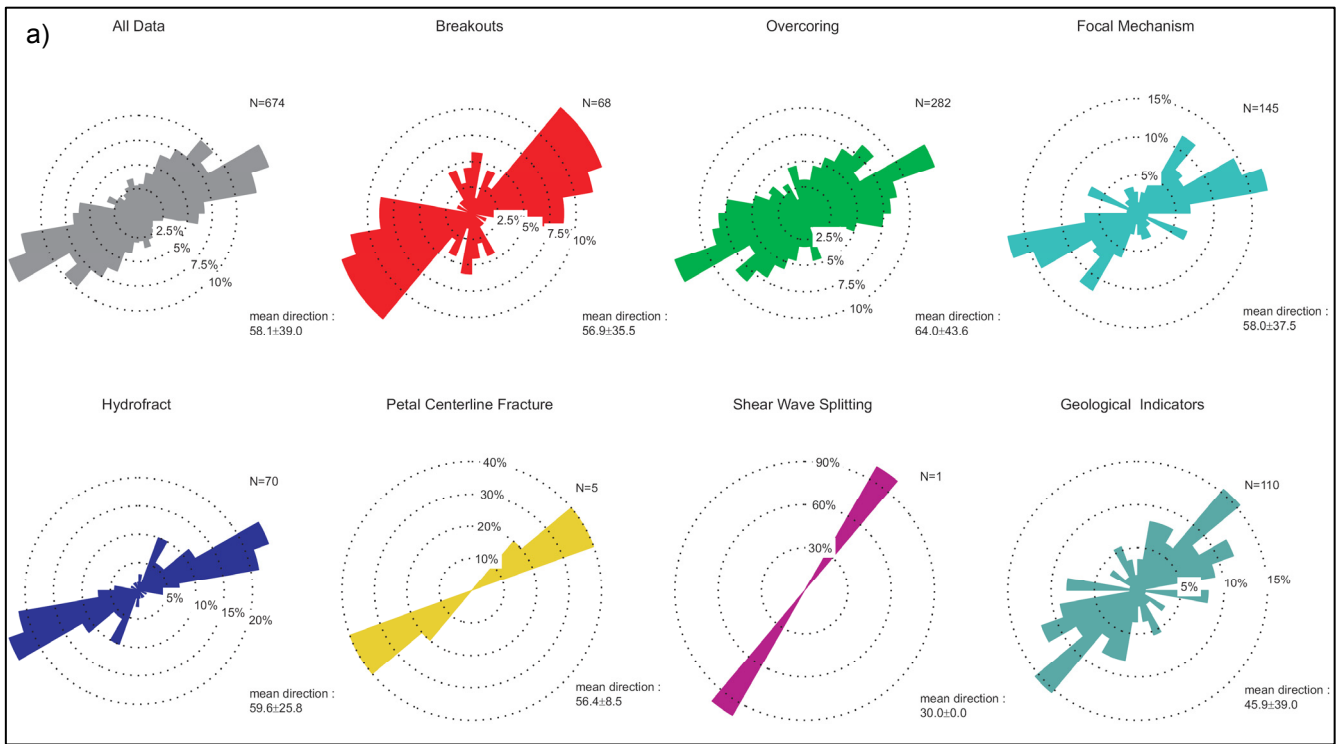
Figure 16   Stress orientation data WSM2008 and Adams databases for the Great Lakes area. a) Circular histograms of S_{Hmax} orientation for all data, breakouts, overcoring, focal mechanism, hyd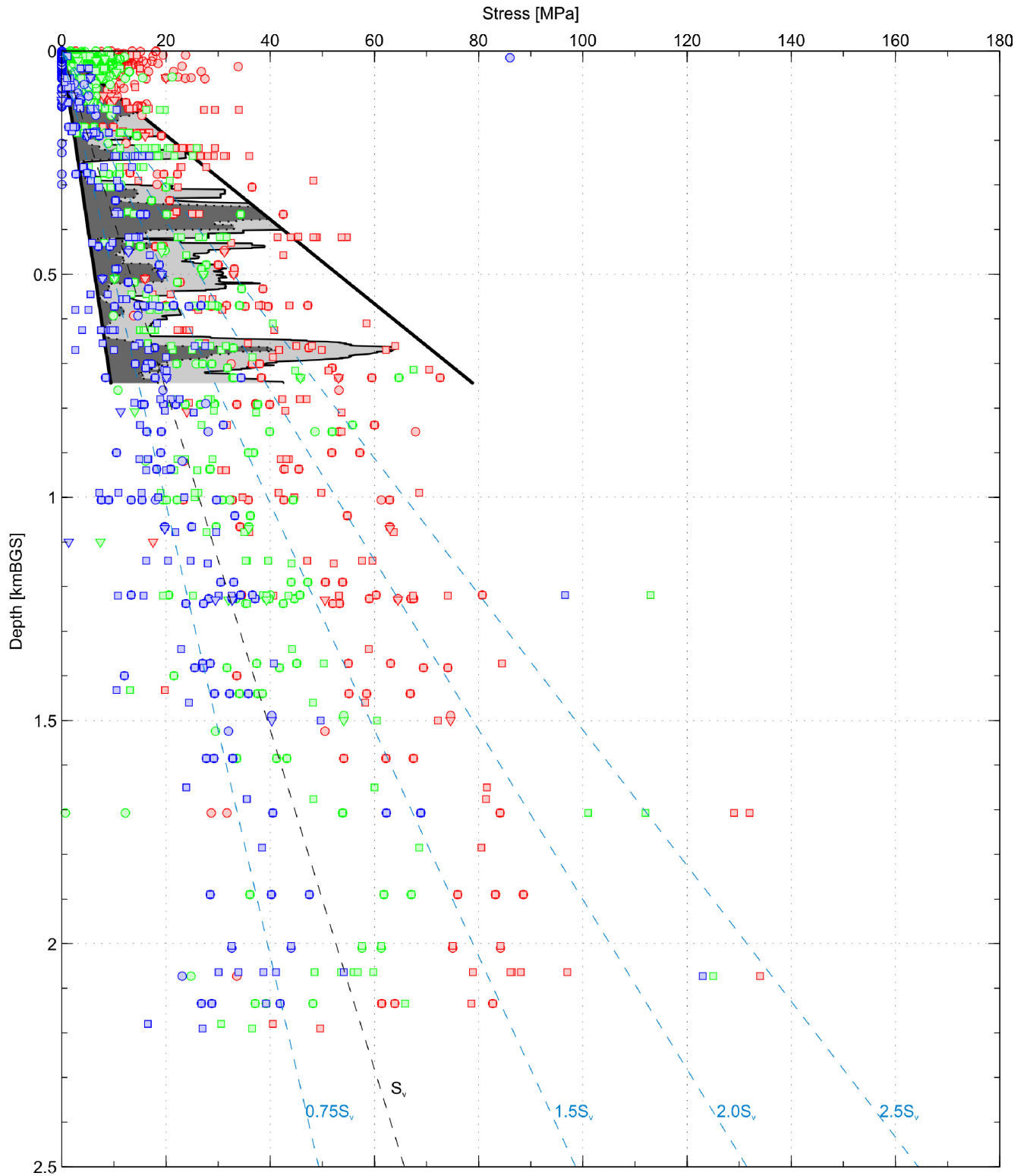rofract, petal centerline fracture, shear wave splitting and geological indicators (mostly pop-ups and floor buckles) from both WSM2008 and Adams databases. b) Circular histograms of S_{Hmax} orientation for all data, breakouts, overcoring, focal mechanism, hydrofract, petal centerline fracture, shear wave splitting from only the WSM2008 database.

Figure 17 Stress magnitude vs. depth. σ_1 in red, σ_2 in green and σ_3 in blue. Adams data base (circles), Maloney database (squares) and WSM2008 data base (triangles). Adams and WSM2008 data is limited to a region surrounding the Great Lakes. Entire Maloney database is included. Constraints given by the stress analysis of Figure 15 are also displayed in the background of the stress data (50% level in light gray and 1% level in darker gray).
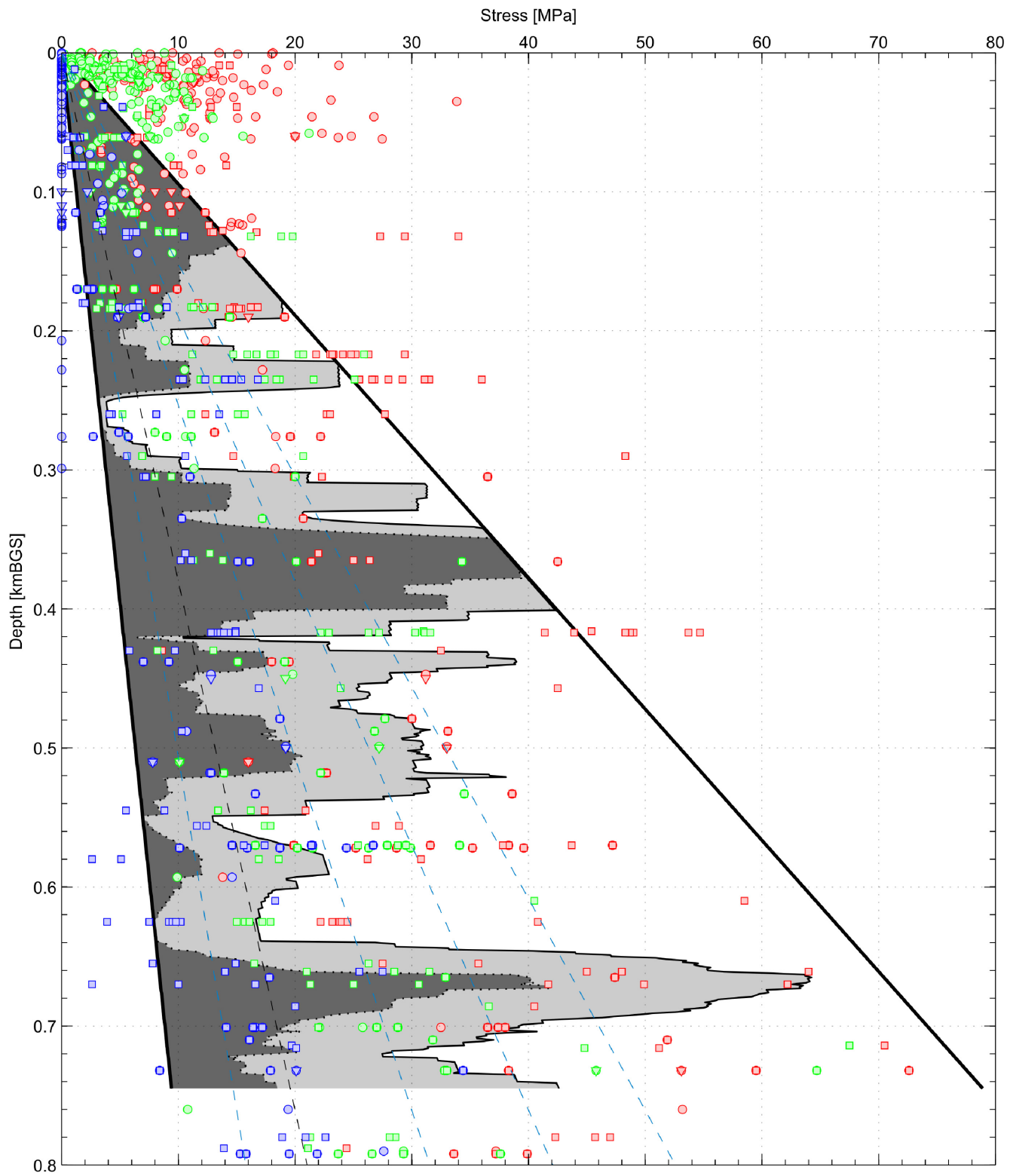
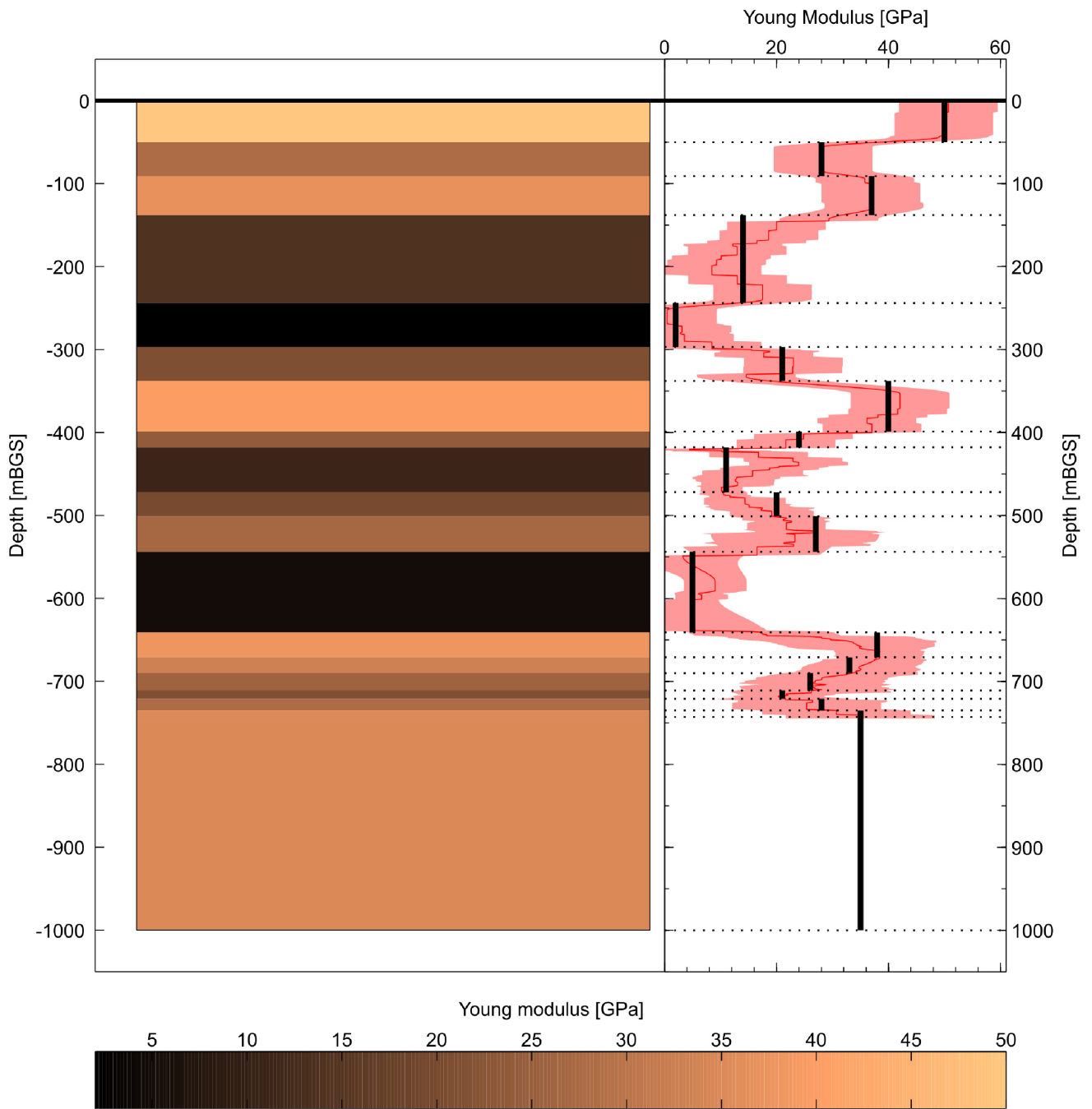Figure 18   Idem to Figure 17, but zoomed on the depth of interest of this study.

Figure 19   Stiffness profile discretized in order to model the possible stress repartition with depth.
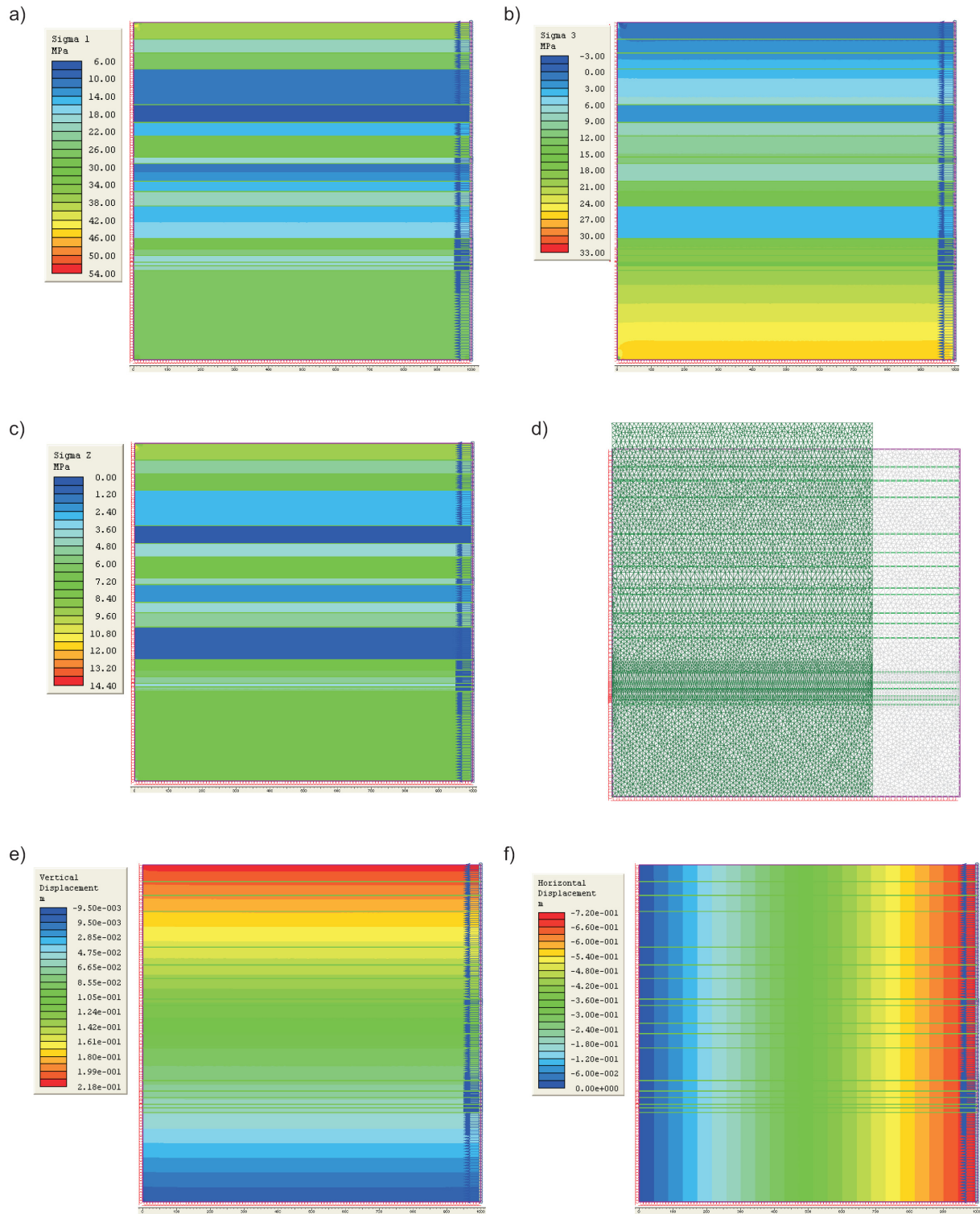
Figure 20 Phase² model for a fixed displacement of 0.7 m. a) maximum stress, b) minimum stress, c) out of plane stress, d) initial (gray) and deformed (green) mesh, e) vertical displacement, and f) horizontal displacement.
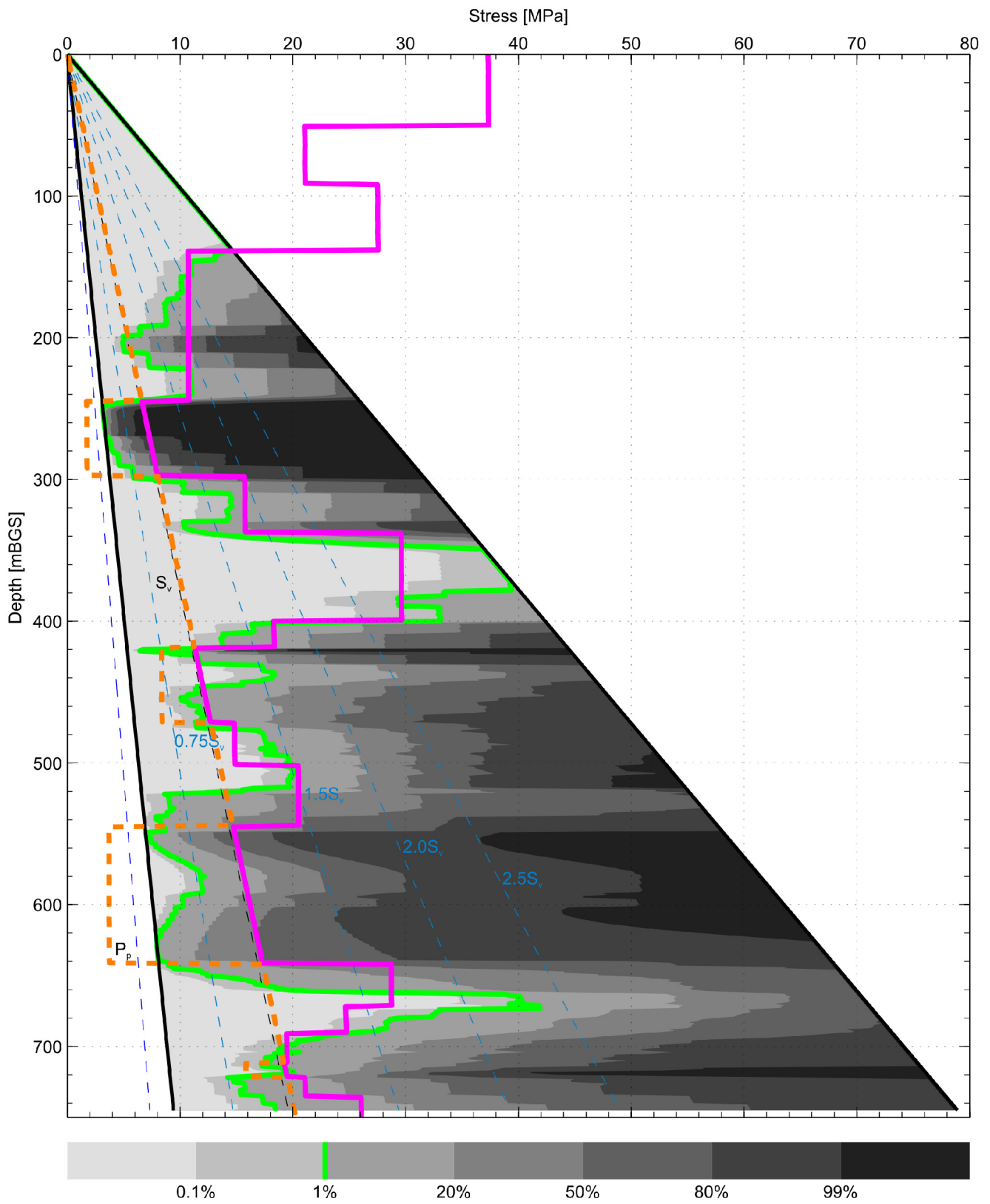
Figure 21   Comparison of phase² model output for a fixed boundary displacement of 0.7 m (σ_1, magenta line, σ_3 orange dashed line) with the constraints set by the absence of borehole failure (green line).